

Characterizing Spin Qubits in Semiconductor Quantum Dots

Bachelor's Thesis Project II

Devashish Shah

Roll no: 200260015

Supervised by

Prof. Suddhasatta Mahapatra



Engineering Physics,
Indian Institute of Technology, Bombay

Acknowledgements

I would like to thank Professor Sudhasatta Mahapatra for his continual support and guidance, academic and otherwise. I am also grateful for the insightful discussions and key lessons in low-temperature measurements I learned from interactions with Professor Sudhasatta Mahapatra and Professor Kantiay Dasgupta.

I would also like to thank the graduate students I worked with. Mr. Sounak Samanta, for the guidance and help with instrumentation and measurements. Mr. Siddarth Rastogi and Ms. Varsha Jangir for sharing their knowledge of nano-fabrication and for their persistent effort toward the fabrication of the devices measured. Mr. Bikash C. Barik for the regular guidance with details regarding the quantum transport experimental setup.

Abstract

The field of quantum computing is currently led by superconducting transom qubits, with the industrial research groups having achieved noisy intermediate-scale quantum (NISQ) processors with 1000+ physical qubits. Despite this, superconducting qubits face fundamental roadblocks in terms of scaling, short-lived quantum states, and so on. Semiconductor spin qubits have emerged as a promising platform for realizing robust qubits boasting long coherence times and fast qubit operations. With a very small lithographic footprint compared to superconducting qubits, semiconductor spin qubits are also very good candidates for the scalability of the platform in the long run,

This thesis focuses on measurements characterizing nanometer-scale gate-defined quantum dots in a Gallium Arsenide quantum well. A single electron spin confined in such a tunable electrostatic potential is a promising candidate for a quantum bit. Starting from the characterization of the quantum well using transport measurements, we demonstrate the ability to selectively “tune” single and coupled quantum dots in an eight-quantum-dot array while setting up and optimizing critical electronic measurement techniques.

Contents

1 Semiconductor Spin Qubits	5
1.1 Introduction	5
1.2 DiVincenzo criteria	6
1.3 Loss DiVincenzo Spin Qubit	7
2 Device Design	14
2.1 Band Engineering	14
2.2 Quantum Dot Device	16
2.2.1 Overview	16
2.2.2 Fabrication	17
2.2.3 Notation	19
3 Characterizing the Quantum Well	20
3.1 GaAs AlGaAs Hall Bar	21
4 Transport Through Single Quantum Dots	26
4.1 The Constant Interaction Model	26
4.2 Coulomb Spectroscopy	28
4.3 Charge Sensing	30
4.4 Measurements on SQDs	31
4.4.1 Tuning a SQD	31
4.4.2 Electron Temperature	34
4.4.3 Going down to the Last Electron	38
5 Double Quantum Dots	39
5.1 Constant Interaction Model	39
5.2 Measurements on DQDs	41

5.2.1	Tuning a DQD	41
6	Spin Readout and T_1 measurement	44
6.1	Elzerman Spin readout (ERO)	44
6.1.1	T_1 Measurement using ERO	44
6.2	Pauli Spin Blockade	45
7	Experimental Setup	49
7.1	Dilution Fridge	49
7.1.1	Working Principle [1]	49
7.1.2	Setup	51
A	Appendix	53
A.1	Quantum Hall Effect	53
A.2	Reflectometry	57
A.3	QCoDeS	59

Chapter 1

Semiconductor Spin Qubits

1.1 Introduction

The intrinsic spin magnetic moment of an electron is a purely quantum mechanical property arising from the spinor algebra of the Dirac equation. This magnetic dipole can be in one of two degenerate eigenstates in the absence of an external field. This degeneracy is broken when a DC magnetic field is turned on. In addition to this, a perturbative oscillating magnetic field can be used to drive oscillations between the two eigenstates. Thus, an electron spin in the presence of a magnetic field is a natural candidate for making a quantum bit: qubit, with spin-up $|\uparrow\rangle$ and spin-down $|\downarrow\rangle$ forming the two orthogonal states constituting the qubit. Harnessing these spin states for applications in quantum information and computing is an aspect this thesis focuses on. Although the field of experimental quantum computing is relatively young, magnetic properties arising from this intrinsic spin magnetic moment of Fermions, have been exploited extensively, with memory devices, magnetic read leads, and medical imaging (MRI) being a few examples. All of these applications rely on the manipulation and measurement of the net magnetization vector of a material using an external field. Despite the intrinsic spin of an electron (or nuclear spin of atoms) being a purely quantum mechanical property, in nearly all practical cases where one works with a large ensemble of spins, the quantum state decoheres so rapidly that no quantum effects can be observed. One effectively takes into consideration the net magnetization vector, which behaves like a classical magnetic moment.

To be able to observe and manipulate the quantum state of electron spins, one needs

a system where a few spins can be isolated at very low temperatures. Electron spins confined in *gate-defined semiconductor quantum dots*, cooled down to cryogenic temperatures, is one such system. To understand why these are good qubit candidates, a natural starting point is revisiting the DiVincenzo criteria.

1.2 DiVincenzo criteria

In 1998, Daniel Loss and David P. DiVincenzo [16] proposed an implementation of universal one and two-qubit quantum gates for quantum computation using spin states of coupled single-electron quantum dots, followed by a work by Daniel P. DiVincenzo in 2000 [4], which laid down the preliminary requirements for realizing functional qubits for quantum computation. The *DiVincenzo criteria* can be summarized as follows:

1. **Scalable well characterized qubits:** The physical parameters of the qubit are accurately known, namely its internal Hamiltonian and couplings or interactions with other qubits and the environment. Equivalently, one should be able to fabricate a well-defined two-level quantum system in a reliable, reproducible manner,
2. **High fidelity initialization:** Initializing a qubit (or a qubit array) to a well-defined initial state must be possible at times much shorter than the decoherence time.
3. **Decoherence times much longer than the gate operation time:** The quantum system must remain coherent for times much longer than the duration of execution of logic gates to allow fault-tolerant computation.
4. **Universal set of quantum gates:** It should be possible to execute a universal set of quantum logic gates; the single-qubit Pauli gates, along with the two-qubit CNOT, is one set.
5. **Qubit-specific measurement capability:** Post operation, it should be possible to read out the final state of the qubit array with acceptable fidelity.

In this thesis, we demonstrate the ability to tune single and double quantum dots to the few-electron regime, followed by the capability of charge sensing and spin readout, thus demonstrating criteria 1, 2, and 5.

1.3 Loss DiVincenzo Spin Qubit

Having laid out the criteria that a physical realization of a qubit must meet, it is fruitful to first start with a completely mathematical description of a DiVincenzo spin qubit and how one would drive such a two-level system (criterion 4 in sec 1.2)¹. We start with single electron spins $\vec{S}_i = \frac{\hbar}{2}\vec{\sigma}_i$ mapped to Pauli matrices in an external magnetic field. The Zeeman split spin states form the quantum two-level system. The Hamiltonian describing several such spin qubits coupled to one another is:

$$\hat{H}(t) = \frac{1}{4} \sum_{(i,j)} J_{ij}(t) \vec{\sigma}_j \cdot \vec{\sigma}_i - \frac{1}{2} \sum_i g_i \mu_B (\vec{B}_i^0 + \vec{B}_i(t)) \cdot \vec{\sigma}_i \quad (1.1)$$

The first term is the Heisenberg Hamiltonian with J_{ij} being the exchange coupling between the i^{th} and the j^{th} spin and the second term is the Zeeman term $(-\vec{\mu} \cdot \vec{B}_{tot})$. Time-dependent fields $\vec{B}_i(t)$ and site-based g -factor modulation allow for qubit operations in the presence of a DC Zeeman field. The static fields \vec{B}_i^0 may also be made to vary slightly for each site. The unperturbed Hamiltonian for a single spin in a DC magnetic field $\vec{B} = B_0\hat{z}$ in the σ_z basis is:

$$\hat{H}_0 = \frac{\hbar\omega_L}{2} \begin{bmatrix} -1 & 0 \\ 0 & 1 \end{bmatrix} \quad (1.2)$$

Here, $\omega_L = geB_0/2m^*$ is the Larmor frequency. The eigenstates of the Hamiltonian are $|0\rangle = [1 \ 0]^T$ and $|1\rangle = [0 \ 1]^T$, with eigenvalues $-\hbar\omega_L/2$ and $\hbar\omega_L/2$ respectively. These are the logic LOW and logic HIGH states of the quantum bit. In contrast to a classical bit, any general state vector can be a superposition of these two eigenstates:

$$\psi = \alpha |0\rangle + \beta |1\rangle = \begin{bmatrix} \alpha \\ \beta \end{bmatrix} \quad (1.3)$$

Here $\alpha, \beta \in \mathbb{C}$, and $|\alpha|^2 + |\beta|^2 = 1$, with $|\alpha|^2$ and $|\beta|^2$ being the probability of finding the system in state $|0\rangle$ and $|1\rangle$ respectively. A very convenient visualization of this 2D space spanned by the eigenvectors is the Bloch sphere representation², where $\alpha = \cos(\frac{\theta}{2})$ and $\beta = e^{i\phi} \sin(\frac{\theta}{2})$. An arbitrary state vector in the 2D Hilbert space

¹This section describes an idealized system without getting into complications of state preparation, readout, etc. It is a summary of the physics that lies behind the realization of a universal set of gates for a DiVincenzo qubit [29].

²Global phases of the state $|\psi\rangle$ have no physical implication and can be ignored; thus, here α is taken to be real without loss of generality.

can then be mapped to a unique point on a unit sphere ($\psi = \psi(\theta, \phi)$) called the Bloch sphere.

$$\psi = \cos\left(\frac{\theta}{2}\right) |0\rangle + e^{i\phi} \sin\left(\frac{\theta}{2}\right) |1\rangle = \begin{bmatrix} \cos\left(\frac{\theta}{2}\right) \\ e^{i\phi} \sin\left(\frac{\theta}{2}\right) \end{bmatrix} \quad (1.4)$$

Unitary time evolution of the state $|\psi\rangle$ can be seen as a precession about the z-axis on the Bloch sphere (fig 1.1 (a)):

$$\begin{aligned} \psi(t) &= \cos\left(\frac{\theta}{2}\right) |0(t)\rangle + e^{i\phi} \sin\left(\frac{\theta}{2}\right) |1(t)\rangle \\ &= e^{i\omega_ct/2} \left[\cos\left(\frac{\theta}{2}\right) |0\rangle + e^{i(\phi-\omega_ct)} \sin\left(\frac{\theta}{2}\right) |1\rangle \right] \end{aligned} \quad (1.5)$$

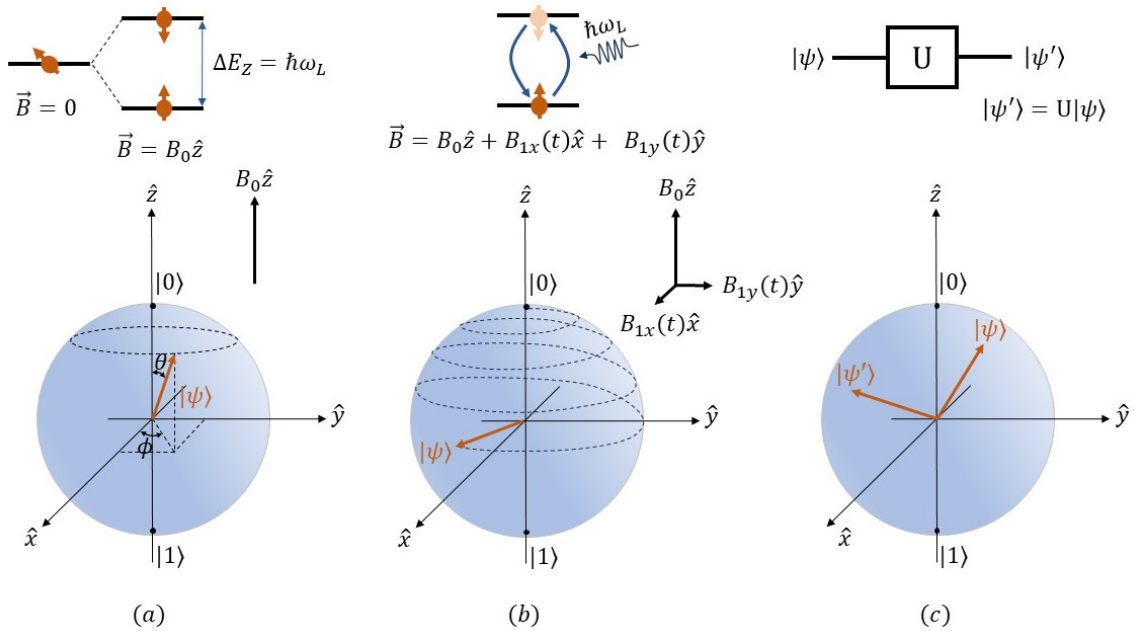


Figure 1.1: (a) Bloch sphere representation of an arbitrary qubit state. (b) Qubit operation using a resonant AC field. (c) A generic unitary operation on a Bloch sphere.

Any unitary operation $|\psi'\rangle = U|\psi\rangle$, where $U^\dagger U = \mathbb{I}_{2\times 2}$, i.e., any single qubit gate, can be shown to correspond to a rotation on the Bloch sphere (section 1.3.1. [20]). For the Hamiltonian in equation (1.2), these unitary operations can be achieved by applying a small oscillating magnetic field perpendicular to the quantization axis.

Driving a Single Qubit

Transitions between the two-qubit levels can be driven using a time-dependent perturbative field $\vec{B}_1(t)$, with $B_1 \ll B_0$. Say, we start with the state $|0\rangle$ at $t = 0$ and

apply a rotating field $\vec{B}_1(t) = B_1 \cos(\omega t)\sigma_x + B_1 \sin(\omega t)\sigma_y$. The state at any time t is then given by $|\psi(t)\rangle = c_0(t)|0\rangle + c_1(t)|1\rangle$. The Hamiltonian of this system is:

$$\begin{aligned}\hat{H} &= \hat{H}_0 + \hat{H}' = -\frac{1}{2}g\mu_B(B_0\sigma_z + B_1 \cos(\omega t)\sigma_x + B_1 \sin(\omega t)\sigma_y) \\ &= -\frac{E_L}{2}|0\rangle\langle 0| + \frac{E_L}{2}|1\rangle\langle 1| - Ve^{-i\omega t}|0\rangle\langle 1| - Ve^{i\omega t}|1\rangle\langle 0|\end{aligned}\quad (1.6)$$

$E_L = \hbar\omega_L$ and $V = g\mu_B B_1/2$. This is one of the few exactly solvable problems in time-dependent perturbation theory ($i\hbar \dot{c}_m(t) = \sum_n c_m(t) \langle m | H' | n \rangle e^{i\omega_{mn}t}$). The solution to this problem is:

$$|c_1(t)|^2 = \frac{V^2/\hbar^2}{V^2/\hbar^2 + (\omega - \omega_L)^2/4} \sin^2 \left\{ \left[\frac{V^2}{\hbar^2} + \frac{(\omega - \omega_L)^2}{4} \right]^{1/2} t \right\} \quad (1.7)$$

$$|c_0(t)|^2 = 1 - |c_1(t)|^2 \quad (1.8)$$

The probability of finding the higher energy state oscillates with frequency two times that of $\Omega = \left[\frac{V^2}{\hbar^2} + \frac{(\omega - \omega_L)^2}{4} \right]^{1/2}$. Equation (1.7) is the Rabi formula and Ω is the Rabi frequency. When the frequency of the oscillating pulse is resonant with the Zeeman splitting, i.e., $\omega = \omega_L$, the oscillation amplitude is maximum and equals one.

A more complete description of the system is one that includes dissipative interactions of the spin qubit with the environment. The total state of the qubit + environment (density matrix ρ_{tot}) then evolves according to the von Neumann equation $\dot{\rho}_{tot}(t) = -\frac{i}{\hbar}[\hat{H}_{tot}, \rho_{tot}(t)]$. The state of the system $\rho = Tr_{env}(\rho_{tot})$ obtained by tracing out the environment evolves in accordance to the Lindblad master equation:

$$\dot{\rho} = \mathcal{L}(\rho) = -\frac{i}{\hbar}[\hat{H}(t), \rho(t)] + \sum_n \left[L_n \rho L_n^\dagger - \frac{1}{2} L_n^\dagger L_n \rho - \frac{1}{2} L_n L_n^\dagger \rho \right] \quad (1.9)$$

The first term is the unitary evolution generated by the Hamiltonian. Whereas the second term encompasses interactions with the environment. The operators L_n are called Lindblad operators or quantum jump operators [22]. Each $L_n \rho L_n^\dagger$ term induces one of the possible quantum jumps due to interaction with the environment, while the terms $\frac{1}{2} L_n^\dagger L_n \rho$ and $\frac{1}{2} L_n L_n^\dagger \rho$ are needed to normalize properly in case no jumps occur. Interaction of the qubit with the environment leads to two processes:

1. Relaxation: Decaying to the lower energy (ground) state $|0\rangle$ over time. In the block sphere picture, this means the tipping of the state vector toward the North

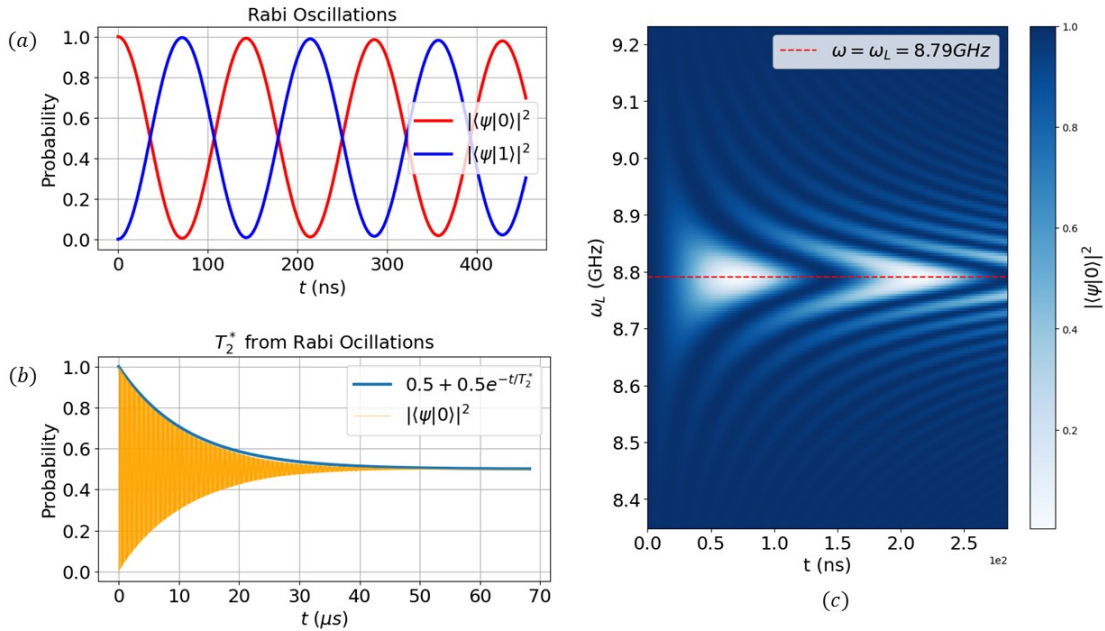


Figure 1.2: Qutip simulations: (a) Rabi oscillations between states $|0\rangle$ and $|1\rangle$. (b) Decaying Rabi amplitude due to decoherence gives a measure of the decoherence time T_2^* . (c) A drive frequency sweep which is used (experimentally) to obtain the Larmor frequency of the qubit. Driving off-resonance gives negligible oscillation amplitude.

Pole. The jump operator for relaxation is:

$$L_1 = \sqrt{\gamma_1} |0\rangle\langle 1| = \sqrt{\gamma_1} \begin{bmatrix} 0 & 1 \\ 0 & 0 \end{bmatrix} \quad (1.10)$$

Here, γ_1 is the relaxation rate. If initialized to $|\psi\rangle_i = |1\rangle$, the probability of finding the system in state $|1\rangle$ decays exponentially, with a time constant T_1 (inversely related to γ_1).

2. Dephasing: The loss of phase coherence of the qubit. This is most conveniently visualized in the Bloch sphere picture as an increasing uncertainty in the azimuthal angle ϕ of the Bloch vector. The jump operator for dephasing is:

$$L_2 = \sqrt{\gamma_2} \sigma_z = \sqrt{\gamma_2} \begin{bmatrix} 1 & 0 \\ 0 & -1 \end{bmatrix} \quad (1.11)$$

Here, γ_2 is the dephasing/decoherence rate. If initialized to $|\psi\rangle_i = \cos(\theta/2)|0\rangle + e^{i\phi}\sin(\theta/2)|1\rangle$ with well-defined phase ϕ , the uncertainty or fuzziness in the phase increases exponentially, with a time constant T_2 (inversely related to γ_2).

In practice, electron spin resonance (ESR) with pulsed AC magnetic fields can be used to execute single-qubit operations. Alternatively, electrically driven spin resonance (EDSR), with pulsed AC electric fields in the presence of spin-orbit interaction or static magnetic field gradients, can be used. Non-entangling two-qubit unitary gate operations, i.e., ones that can be written as a direct product of single-qubit gates $U_{4 \times 4} = A_{2 \times 2} \otimes B_{2 \times 2}$ are just simultaneously driven single qubit operations (with different Larmor frequencies). The local static field or qubit g-factors are tuned such that the two qubits have different Larmor frequencies. Thus, driving one of the qubits at resonance has (almost) no effect on the other.

Entangling Gates

The exchange coupling between two spins in equation (1.1) can be tuned with gate voltages, allowing for the realization of entangling two-qubit gates. In the presence of a non-zero exchange interaction, a two-qubit CNOT operation can be executed using an AC pulse to selectively drive transitions of the target qubit only when the control qubit is in state $|1\rangle$ [fig 1.3]. Here, the system Hamiltonian in the $\{|00\rangle, |01\rangle, |10\rangle, |11\rangle\}$ basis is:

$$\hat{H}(J, B) = \frac{1}{2} \begin{bmatrix} -\Sigma g \mu_B B & 0 & 0 & 0 \\ 0 & -\Delta g \mu_B B - J & J & 0 \\ 0 & J & \Delta g \mu_B B - J & 0 \\ 0 & 0 & 0 & \Sigma g \mu_B B \end{bmatrix} \quad (1.12)$$

Here, $\Sigma g = g_1 + g_2$ is the sum of electron g-factors at the two sites, and $\Delta g = g_1 - g_2$ is the difference. J is the exchange interaction term. Again, the time evolution of the system driven at a particular frequency is obtained by solving the corresponding Lindblad master equation (1.9)¹.

Experimentally, the exchange interaction between spins confined in coupled quantum dots is controlled by varying the tunneling rate between the two quantum dots. In most cases, the oscillatory excitations are AC electric fields applied to the plunger or barrier gates of the corresponding quantum dot. Due to spin-orbit interaction, these

¹The jump operators in the two-qubit computational basis are constructed by taking the appropriate tensor product of single qubit collapse operators with identity and with one another (both qubits assumed to decohere at the same rate independently of one another).

AC electric fields are seen as oscillating magnetic fields by the electron spin. In the case of substrates without appreciable spin-orbit interaction, micromagnets are used to generate site-dependent magnetic field gradients, leading to a spin-orbit-like term in the Hamiltonian, allowing for full electric control of the spin qubit [28].

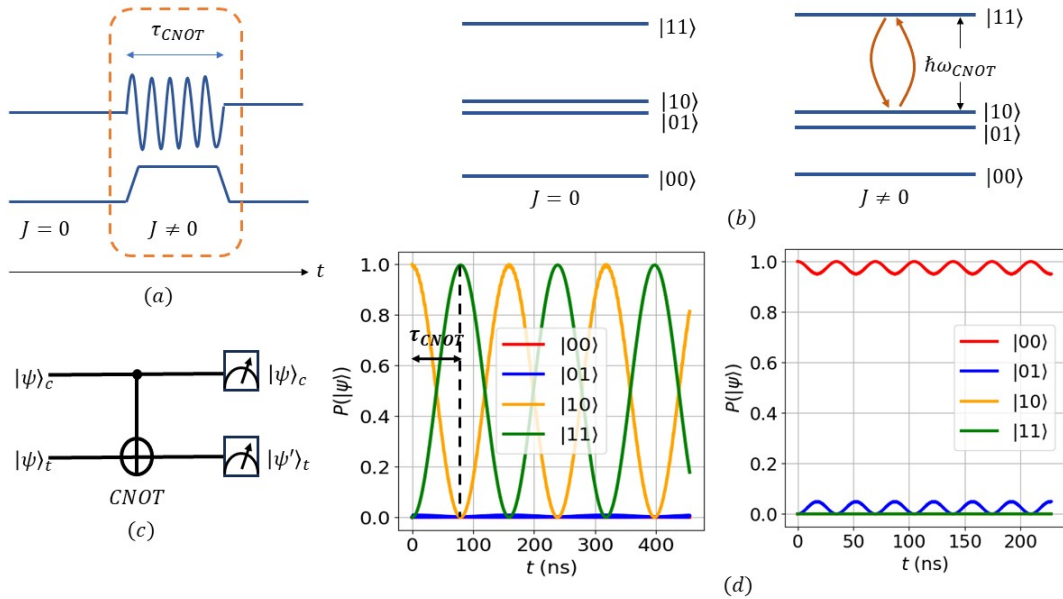


Figure 1.3: (a) Pulse sequence for executing a CNOT gate. The CNOT operation is executed by driving the qubit at ω_{CNOT} for a pulse duration of τ_{CNOT} . (b) Tuning of the two-qubit energy spectrum by controlling the exchange interaction J . (c) Circuit symbol: CNOT gate. (d) Occupation probability of the basis states vs duration of pulse: Qutip simulations for the time evolution of a two-qubit system (with exchange interaction) driven at $\hbar\omega_{CNOT}$. Here, a CNOT gate can be executed by choosing pulse duration τ_{CNOT} . Small amplitude off-resonance oscillations are seen even when the control qubit is in state $|0\rangle$, which can be eliminated by fine-tuning J and g -factors.

Simulation results in figure (1.3) and figure (1.2) are for a toy model of spin(s) in a DC field of 0.5T. An AC drive field at the appropriate frequency (depending on which two levels are driven) of amplitude 10mT is used to drive the two-level system. The decoherence rate γ_1 corresponding to $T_2^* \simeq 30\mu s$ is used ($T_1 \sim 100T_2$). The g-factors are taken to be different ($g_1 = 1.95$ and $g_2 = 2.05$), assuming site-dependent modulation is possible and the effective mass to be $0.1m_e$, where m_e is the free electron mass. In figure (1.3), an exchange interaction J with strength equivalent to a free electron Zeeman splitting at 0.02T is included in the Hamiltonian. Further interaction

terms like spin-orbit terms, hyperfine, etc. can be simply added in the Hamiltonian [eq 1.12] to understand experimental results in specific cases.

Chapter 2

Device Design

2.1 Band Engineering

The fundamental design of gate-defined quantum dot devices in semiconductor heterostructures is derived from that of a MOSFET, with a key difference being the channel depth. Clever band engineering combined with high-quality molecular beam epitaxy is used to “grow” heterostructures where electron confinement in the direction of growth is possible. The GaAs|AlGaAs heterostructures we use consist of four main semiconductor layers - a 5nm GaAs cap layer, 40nm modulation-doped Al_{0.33}Ga_{0.67}As:Si layer, 40nm spacer Al_{0.33}Ga_{0.67}As layer, and the ~1000nm GaAs layer. The conduction band bending along the growth direction leads to the formation of a triangular quantum well at the AlGaAs | GaAs interface, populated by carriers from the modulation-doped AlGaAs:Si layer. The band profile can be obtained by iteratively solving the Schrödinger and Poisson equations with appropriate boundary conditions.

Schrödinger Poisson

The Poisson equation in a solid reads:

$$\vec{\nabla}^2 \phi(\vec{r}) = \frac{e}{\epsilon_0 \kappa} \left[N_D^+(\vec{r}) - N_A^+(\vec{r}) + \sum_{\nu} |\psi_{\nu}(\vec{r})|^2 \mathcal{F}(\varepsilon_{\nu}, \varepsilon_F) \right] \quad (2.1)$$

Here, $\phi(\vec{r})$ is the smooth electrostatic potential, i.e., the potential due to unbalanced charges, excluding the discrete jumps due to the conduction band offsets between GaAs and AlGaAs. κ is the dielectric constant in the semiconductor, $N_D^+(\vec{r})$ and $N_A^+(\vec{r})$ the density of ionized donors and acceptors respectively, $\psi_{\nu}(\vec{r})$ the wavefunc-

tion of electrons in the ν^{th} subband, and $\mathcal{F}(\varepsilon_\nu, \varepsilon_F)$ is the Fermi-Dirac distribution. ψ_ν is obtained by solving the Schrödinger equation with appropriate boundary conditions:

$$\left[-\frac{\hbar^2}{2m^*} \vec{\nabla}^2 \phi(\vec{r}) + V_b(z) - e\phi(\vec{r}) \right] \psi_\nu = \varepsilon_\nu \psi_\nu(\vec{r}) \quad (2.2)$$

Here $\phi(\vec{r})$ is used. Thus, in practice, eqn. 2.1 and eqn. 2.1 are solved iteratively, starting with a “good” guess for ϕ . The boundary conditions imposing continuity and differentiability at the interfaces, along with the bulk values far from the interfaces, allow for self-consistent solutions for ϕ and ψ until satisfactory convergence conditions are met after several iterations. Assuming translation invariance perpendicular to the direction of growth, eqn. 2.1 and eqn. 2.1 can be reduced to differential equations in a single variable z . The 1D Poisson solver developed by Prof. Gregory Snider [24] is a software developed to solve such a problem.

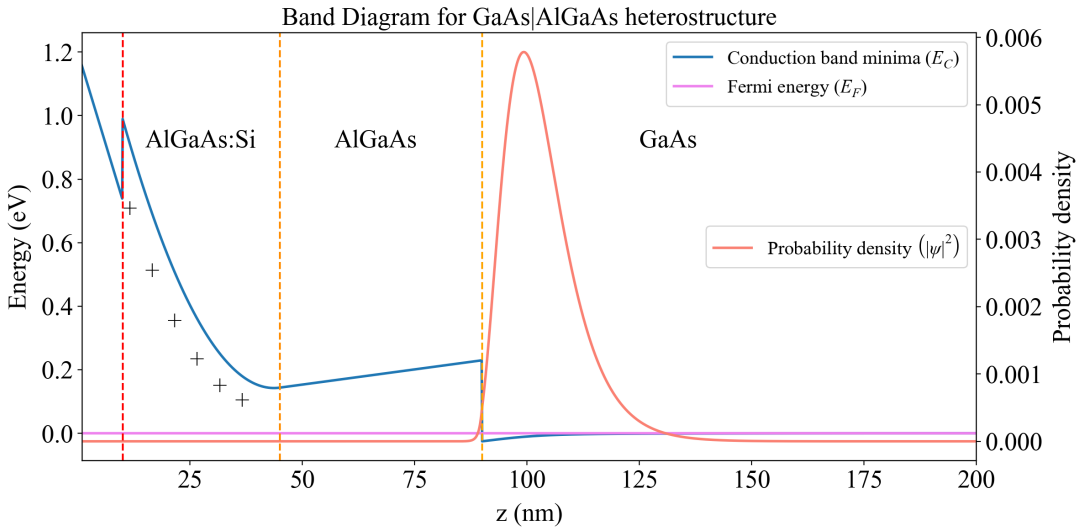


Figure 2.1: Band bending obtained using Prof. Gregory Snider’s 1D Schrödinger-Poisson solver for a nominally similar stack of GaAs|AlGaAs.

The design parameters are chosen such that only one subband in the triangular quantum well formed at the interface is occupied at low temperatures [Fig. 2.2]. AlAs ($a = 5.6531\text{\AA}$) and GaAs ($a = 5.6622\text{\AA}$) have a lattice mismatch of less than 0.5%, allowing for a very stable alloy and nearly ideal heterojunctions with minimal strain. This, along with the increased separation of the quantum well from the surface, has allowed growth of extremely high-quality structures [18] with mobilities of the order of $\sim 10^6 \text{ cm}^2/\text{Vs}$ for sheet densities around $\sim 10^{11} \text{ cm}^{-2}$ in the quantum well.

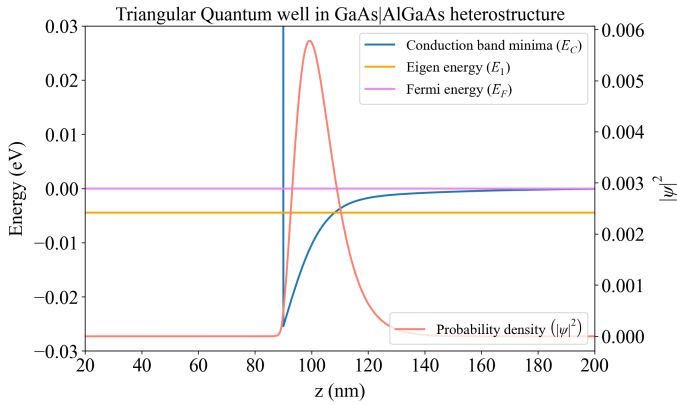


Figure 2.2: Zoom in the region around the triangular quantum well in Fig. 2.1. Only one subband is occupied.

2.2 Quantum Dot Device

2.2.1 Overview

Spin qubits in semiconductor heterostructures require strong 3D electrostatic control to be able to confine a few electrons in a well-defined spatial region. Confinement along the direction of growth, say the z-axis, is already provided by the formation of a triangular quantum well with a single occupied subband, forming a 2D electron gas (2DEG). Confinement in the 2DEG (x-y plane) plane is achieved using voltages applied to surface gates [Fig. 2.3c]. The cumulative effect of these gates can be used to confine a few electrons in regions with sub-100 nm diameters - *quantum dots*. These gate-defined quantum dots are essentially artificial atoms with discrete tunable energy states.

We work with an eight quantum dot array on a GaAs|AlGaAs heterostructure adopted from the work by C. Volk et al. [26]. At the QSi lab, we aim to demonstrate two-qubit universal gating and spin-photon coupling in a Si|SiGe platform soon. Despite Si qubits being much better than GaAs in terms of decoherence rates, we first intend to set up and optimize the measurement apparatus on a GaAs quantum dot array, the reasons being multifold:

1. GaAs has a much smaller effective mass than Si ($0.067m_0$ compared to $0.19m_0$ transverse effective masses); thus, the lithographic features can be larger, i.e., stronger confinement is required for Si.

2. Appreciable spin-orbit interaction in GaAs allows for all electrical qubit control, i.e., electrically driven spin resonance (EDSR).
3. Modulation-doped GaAs heterostructures need a single layer of top gates compared to three layers in the case of Si, where 2DEG accumulation also needs gating.
4. Possibility of studying hall physics in quantum dots in a strong magnetic field perpendicular to the 2DEG.
5. Scope for implementing ML algorithms for tuning up a large quantum dot array.

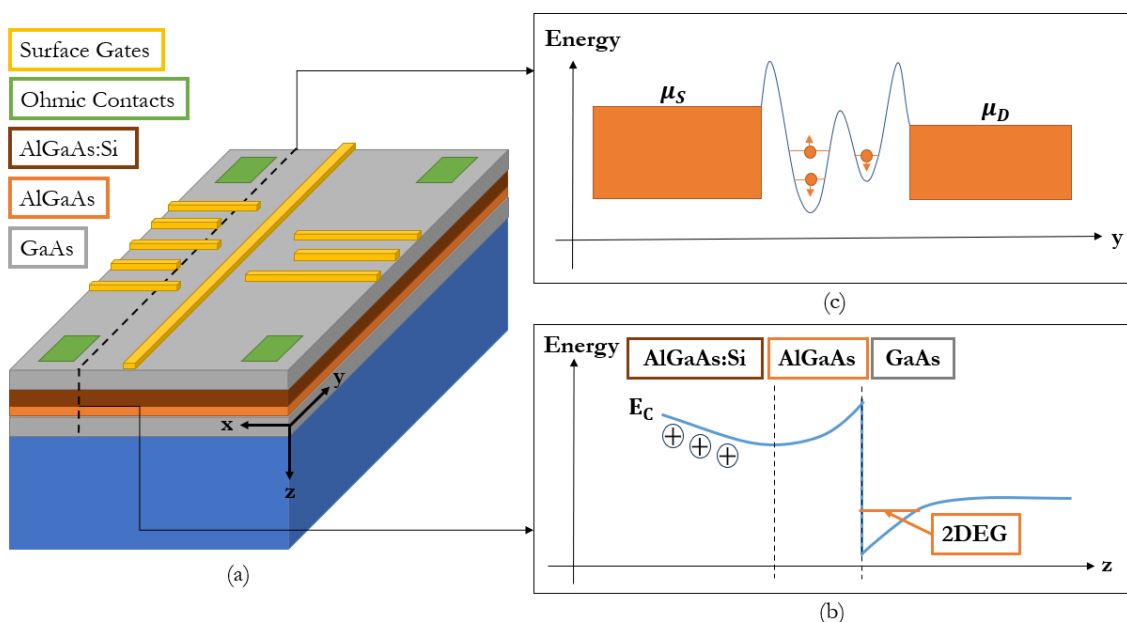


Figure 2.3: (a) A schematic of the structure for a GaAs|AlGaAs spin qubit device. (b) Band bending along the direction of growth. The quantum well formed at the AlGaAs|GaAs interface is populated by electrons from the Si-doped AlGaAs layer. (c) The potential landscape along the plane of the 2D electron gas is manipulated using surface gates.

2.2.2 Fabrication

¹ The fine gate feature size for semiconductor quantum dot devices requires precision down to a few nanometers. With multiple variable parameters in each fabrication step,

¹I would like to thank Ms. Varsha Jangir and Mr. Siddarth Rastogi for sharing their nano-fab knowledge. This section is intended to be a short summary of my understanding of the key steps involved in nanofabrication.

getting good device yield requires not just cutting-edge fabrication techniques but thorough optimization of each step involved in the process. Following is a summary of the key fabrication steps for the GaAs|AlGaAs quantum dot device:

1. Sample cutting and cleaning using RCA: a standard procedure for removal of organic residue from wafers.
2. Resist spinning followed by photo-lithography: the marker design pattern is written onto the wafer.
3. Metallization: Ti-Au deposition on marker regions using electron beam evaporation.
4. Liftoff: NMP removal at 70°C.
5. Mesa Etching: mesa etching is used to etch out regions besides the main device (fine gate and Ohmic area) using diluted Piranha solution (1 : 4 : 100 HCl : H₂O₂ : H₂O).
6. Ohmic contacts are formed by thermal diffusion of Gold-Germanium (AuGe) till the depth of the quantum well, using annealing.
7. Resist spinning followed by photo-lithography: the larger contact leads and pads connecting to the fine gates are written onto the wafer.
8. Metallization: Ti-Au deposition on marker regions using electron beam evaporation.
9. Liftoff: NMP removal at 70°C.
10. Resist spinning followed by electron beam lithography (EBL) to write fine gate pattern.
11. Metallization: Ti-Au deposition on gate pattern using electron beam evaporation
12. Liftoff: NMP removal at 70°C.

The quantum dot device consists of an eight-dot array on one side, with two larger single electron transistor charge sensors on the other side separated by a “backbone” gate [Fig. 2.4]. The two SET dots, when formed, are capacitively coupled to quantum

dots on the array side, allowing for high-precision sensing of the charge state of the quantum dots on the array side.

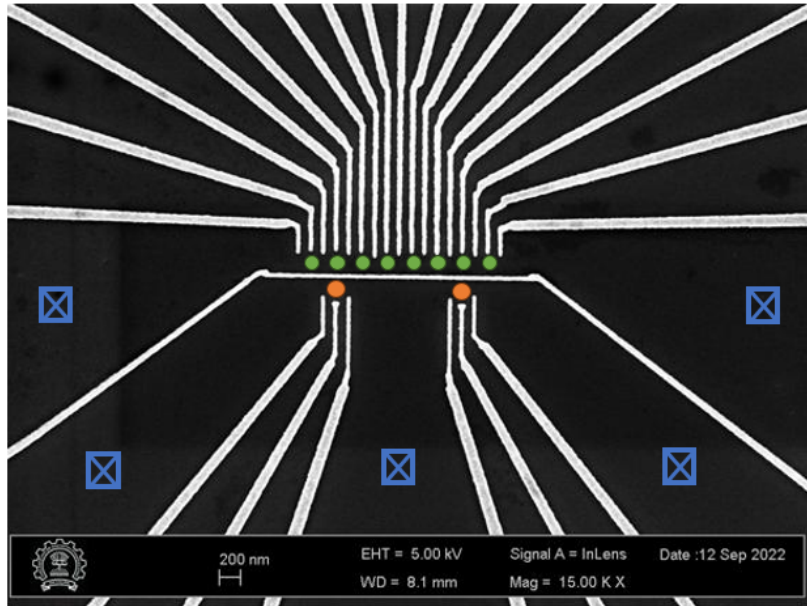


Figure 2.4: Scanning electron microscope (SEM) image of the fine gates of the GaAs quantum dot array. Ohmics are depicted in blue, quantum dots on the array side in green, and SET dots in orange.

2.2.3 Notation

The dots in the array are labeled 1 through 8 from left to right. Thus, each plunger gate is denoted by the corresponding dot number (P1 to P8). Barriers coupling dot i to dot j are denoted by B_{ij} , and the outermost barriers of the array are labeled BL (left) and BR (right). The sensor side gates are labeled as BLCS_i, BRCS₁, and PCS_i for the barriers and plungers of the i^{th} sensor, respectively.

Chapter 3

Characterizing the Quantum Well

The parameters of this 2D electron gas (2DEG), like the carrier density (n), mobility (μ), and the contact resistance with the Ohmic pads (R_C) via implantation pockets, are crucial for transport measurements through quantum dots. The most ubiquitous technique to extract accurate values of these parameters is studying the transverse and longitudinal resistance of a Hall sample in the presence of magnetic fields. In this section, the focus is on experimental results and their analysis. A more rigorous discussion on the Quantum Hall effect can be found in the appendix A.

Lock-in Amplifiers (LIAs) are used for low noise measurements of transverse Hall voltage and longitudinal voltage showing Shubnikov-de Haas (SdH) oscillations. Frequencies (f) chosen for LI measurements are below 100Hz and are such that they are not integer multiples or factors of the 50Hz line frequency. The overall setup is similar to a standard 4-probe setup with the addition of pads to measure transverse voltage. Figure (3.1) is a schematic of the experimental setup. One LIA is used to supply source-drain current indirectly ($I_{SD} = \frac{V_{osc}}{2R_I}$) via a 1:1 isolation transformer and resistances R_I connected to the oscillator output (V_{osc}). $R_I = 10 M\Omega$ is chosen for our setup since it is much larger than the two-probe device resistance, making a near-ideal current source capable of sourcing up to 250 nA. The second LIA is “locked” to the reference signal of the source LIA. The two LIAs are used to record longitudinal ($V_{xx} = V_3 - V_1$) and transverse ($V_{xy} = V_5 - V_2$) voltages by measuring the voltage difference between two voltage pads in A-B mode. The time constant of the LIAs is set to be $\sim \frac{10}{f}$ s. The QDevil daughter board used for the above measurements has a low pass filter with $R_{filter} = 1.2 k\Omega$ and $C_{filter} = 1.0 nF$ on each DC line intended to

block RF noise.

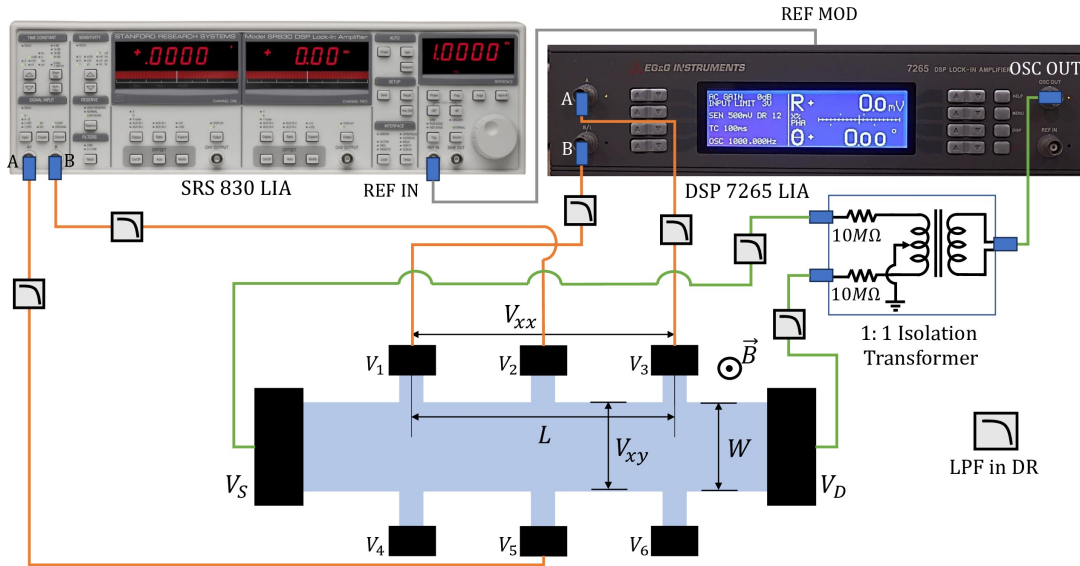


Figure 3.1: Experimental setup for Hall measurements using DSP 7265 and SR 830 LIAs. The Low Pass filter on the QDevil daughter board PCB has a $\frac{1}{R_{filter}C_{filter}} = 0.83$ MHz, orders of magnitude higher than the LIA frequency.

3.1 GaAs|AlGaAs Hall Bar

Quantum Hall effect

Measurement setup for the Hall bar sample [fig (3.2)] is analogous to the one discussed above [fig (3.1)].¹ Two LIAs are used to measure transverse and longitudinal resistances. The source-drain current of amplitude 10 nA RMS, is set indirectly as in figure (3.2).

Quantum Hall and SdH measurement data from 0T up to 9T at different MXC temperatures was recorded. A clear temperature broadening of SdH peaks is seen as MXC temperature increases. Plateaus corresponding to integer filling factors $\nu = nh/eB$ [eq A.12] and some fractional filling factor values are observed. Peaks in R_{xx} coinciding with transitions between Hall plateaus are seen. The Klitzing constant [13]

¹The measurements discussed in this section are done on a Hall bar sample provided by Professor Kanti May Dasgupta at IIT Bombay.

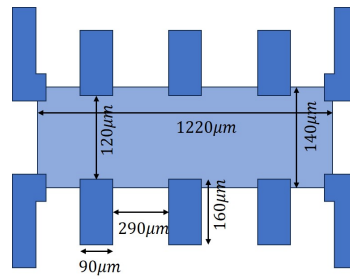


Figure 3.2: Hall sample geometry.

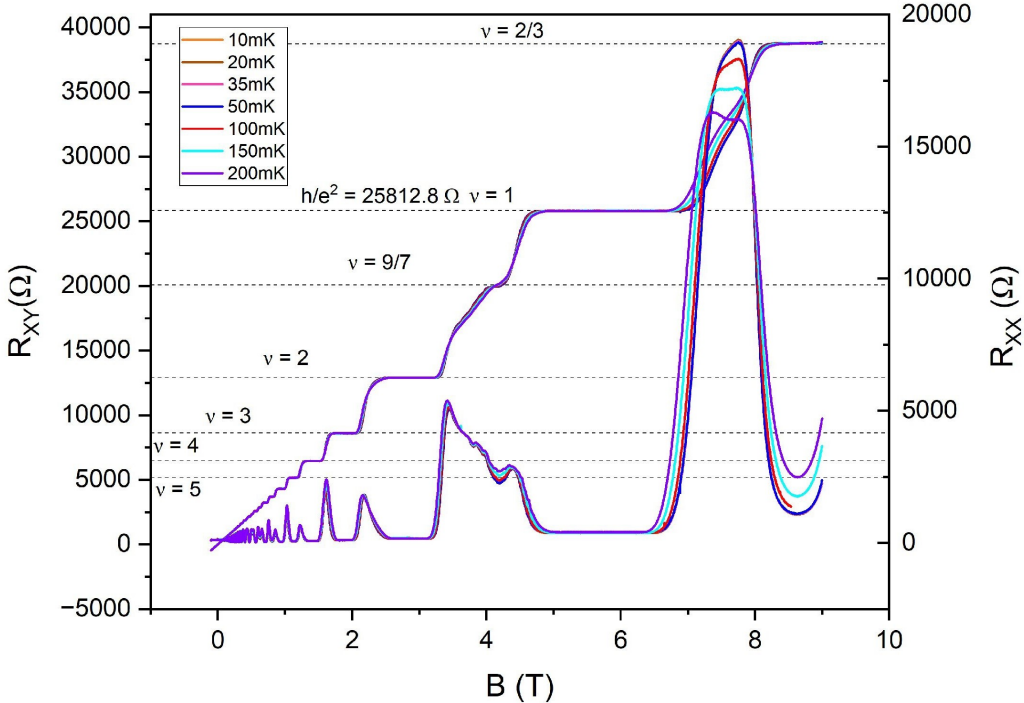


Figure 3.3: Hall and SdH data for a full 0-9T field sweep at different mixing chamber (MXC) temperatures.

$R_K = 25.8128\text{k}\Omega$ (indicated on the plot) allows for the calculation of the actual sample current to be 9.471 nA.

Electron Temperature

As the sample temperature reduces down to the mK regime, the electron-phonon coupling becomes weaker, and the effective electron temperature may differ from the actual lattice temperature, which is thermalized to the cold-finger. The SdH oscillations at intermediate magnetic fields can be used to extract the actual electron temperature using “Dingle fitting” as indicated in [9] and [11]. For intermediate fields,

the amplitude of the SdH oscillations is obtained to be:

$$\Delta\rho_{xx} = 4\rho_0 \frac{\chi}{\sinh\chi} \exp\left[-\frac{\pi}{\omega_c\tau}\right] \quad (3.1)$$

$$\Rightarrow \ln(\Delta\rho_{xx}/4\rho_0) = \ln(\chi) - \ln(\sinh\chi) - \left[\frac{\pi}{\omega_c\tau}\right] \quad (3.2)$$

Here, $\rho_0 = m^*/ne^2\tau$ is the longitudinal resistance at zero field, and $\chi = 2\pi^2k_B T/\hbar\omega_c$ is a parameter that takes into account the effect of the electron temperature and magnetic field. Experimentally, we measure ρ_{xx} as a function of the magnetic field. From the Hall measurement, we can also extract the number density n . We then do a non-linear curve fit in accordance with equation (3.2) [fig 3.6] to optimize for two free parameters, namely τ the relaxation time and electron temperature T .

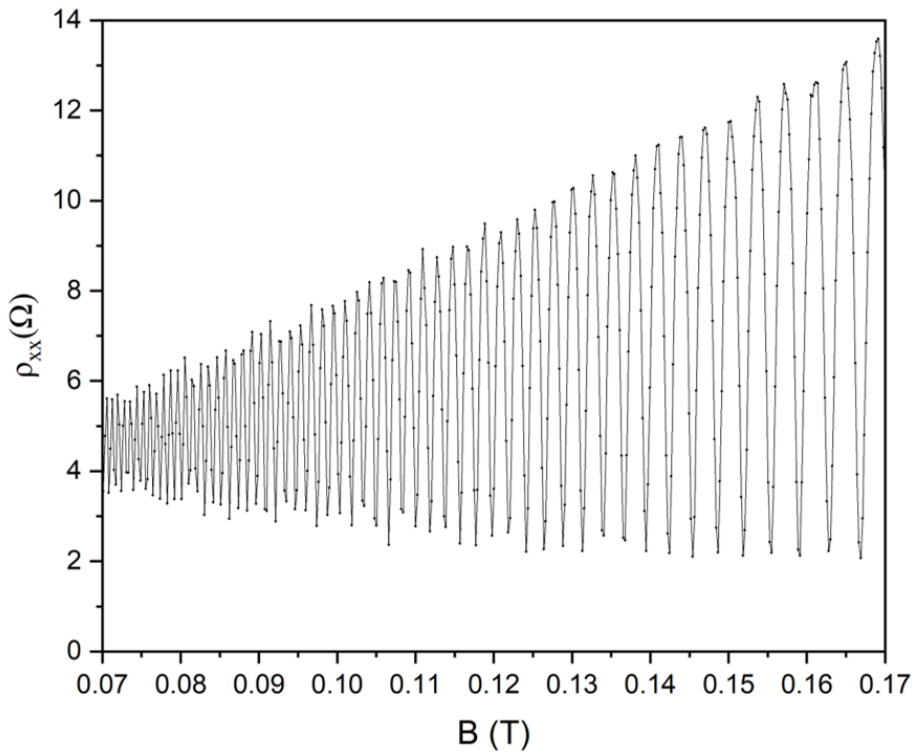


Figure 3.4: (a) Measured SdH oscillations. An envelope is fitted to this data using maxima and minima of the oscillations to obtain $\Delta\rho_{xx}$.

The thermalization of electrons with the lattice can be improved by increasing the number density of electrons in the 2DEG. In the case of GaAs|AlGaAs heterostructures, this can be done by exciting carriers trapped in the DX centers via infrared excitation. This is done using an infrared LED mounted on the coldfinger. A decrease in $|T_{MXC} - T_{electron}|$ is observed post illumination.

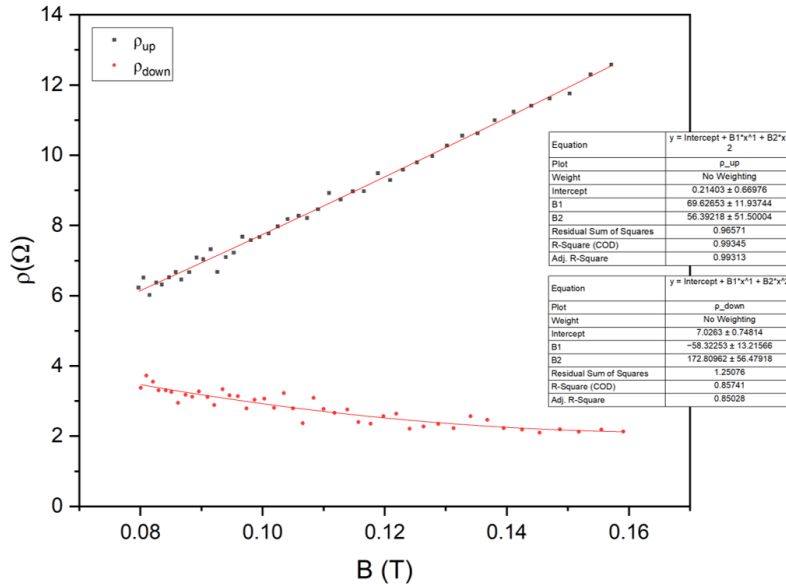


Figure 3.5: Envelope functions for the SdH oscillations (at 10mK) which are used to obtain ρ_{xx} .

Other sample parameters, namely the carrier density (n), and mobility (μ), are obtained from the low field Hall data. The slope of the Hall resistance R_{xy} vs field B gives the number density as $R_{xy} = B/ne$. The mobility $\mu = \frac{1}{\rho_0 ne}$ is then calculated using the zero field longitudinal resistivity $\rho_0 = R_{xx}(B = 0) \cdot W/L$. Here, $W = 140\mu m$ and $L = 670\mu m$. Measured values are (at 10mK MXC):

1. Prior to IR LED illumination: $n = 1.36 \cdot 10^{11} \text{ cm}^{-2}$ and $\mu = 1.78 \cdot 10^6 \text{ cm}^2/\text{Vs}$.
2. Post IR LED illumination: $n = 3.31 \cdot 10^{11} \text{ cm}^{-2}$ and $\mu = 4.67 \cdot 10^6 \text{ cm}^2/\text{Vs}$.

T_{MXC} (mK)	Before Illumination			After Illumination		
	T_e (mK)	$T_e - T_{\text{MXC}}$ (mK)	τ (ps)	T_e (mK)	$T_e - T_{\text{MXC}}$ (mK)	τ (ps)
10	152.3	142.3	4.44	146.0	136.0	7.73
50	163.8	113.8	4.50	133.7	83.7	7.80
100	177.6	77.6	4.50	120.9	20.9	6.90
150	204.3	54.3	4.54	160.7	10.7	7.64
200	226.0	26.0	4.77			

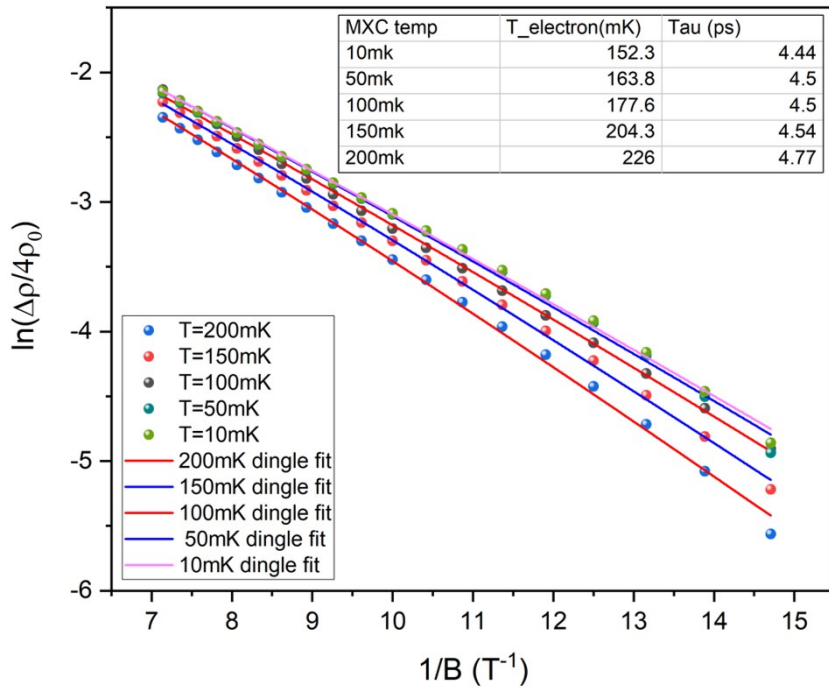


Figure 3.6: Dingle fit for electron temperature and relaxation time τ prior to illumination.

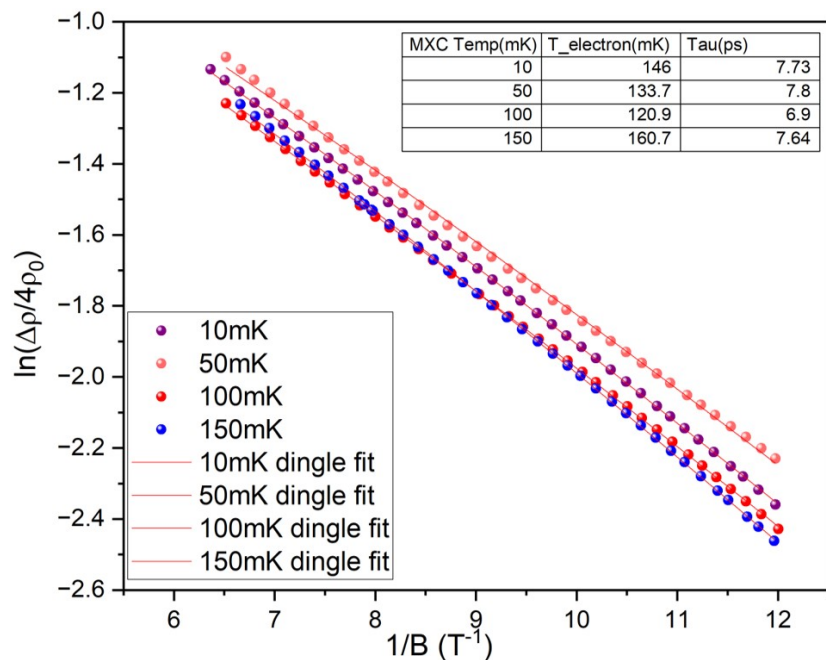


Figure 3.7: Dingle fit for electron temperature and relaxation time τ post illumination.

Chapter 4

Transport Through Single Quantum Dots

4.1 The Constant Interaction Model

A quantum dot is an artificial 3D confinement of electrons in a region of size $\sim 100\text{nm}$ (for semiconductor quantum dots). When the de Broglie wavelength of these electrons is comparable to the size of the dot, they occupy discrete quantum levels similar to orbitals in atoms that have a discrete energy spectrum. Such a quantum dot can be modeled as an island of a finite number of electrons coupled to two reservoirs and a gate, which is used to manipulate the charge state of the quantum dot [Fig.4.1].

The transport through a quantum dot can be understood using the Constant Interaction model [14]. The model is based on two assumptions. First, the interactions of electrons in the quantum dot with the environment are captured by a single effective capacitance $C_\Sigma = C_g + C_s + C_d$, where C_g is the capacitive coupling with the gate, C_s to the source, and C_d to the drain. Second, the single-particle energy spectrum of the dot is independent of the number of electrons. In that case, the energy of the dot filled with N electrons is given by:

$$U(N) = \frac{[-|e|(N - N_0) + C_s V_s + C_d V_d + C_g V_g]^2}{2C_\Sigma} + \sum_{n=1}^N E_n(B) \quad (4.1)$$

Here, $-|e|$ is the electronic charge, and N_0 is the number of electrons at zero gate voltage. $E_n(B)$ if the n^{th} single particle energy state in the presence of an external magnetic field B . The terms $C_i V_i$ ($i = g, s, d$) are effective induced charges due to a

change in the electrostatic potential of the dot. The above expression can be modified to include couplings with other gates and the 2DEG.

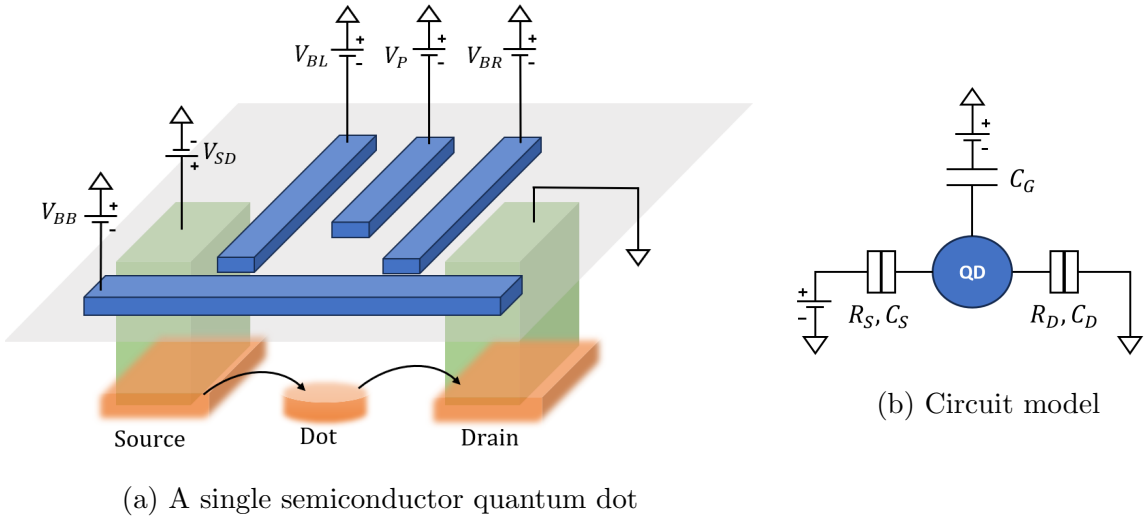


Figure 4.1: The quantum dot is modeled as a conducting island coupled to two reservoirs and four gate electrodes used to deplete the 2DEG by applying negative voltages. The barrier gates (BL and BR) determine the tunnel couplings Γ_S and Γ_D to the reservoirs, and the backbone (BB) in our device divides the 2DEG into two halves. The applied bias $\mu_S - \mu_D = -eV_{SD}$ allows for charge transport when a dot level is in the bias window. The plunger gate is used to control the dot levels.

The electrochemical potential of the dot is defined as:

$$\mu_{N-1 \leftrightarrow N} = U(N) - U(N-1) = E_N(B) + \frac{e^2}{C_\Sigma} \left(N - N_0 - \frac{1}{2} \right) - \frac{e}{C_\Sigma} (C_g V_g + C_s V_s + C_d V_d) \quad (4.2)$$

$$\begin{aligned} \mu_{N-1 \leftrightarrow N} &= E_N + E_C \left(N - N_0 - \frac{1}{2} \right) - \frac{E_C}{e} (C_g V_g + C_s V_s + C_d V_d) \\ &= E_N + E_C \left(N - N_0 - \frac{1}{2} \right) - e \sum_i \alpha_i V_i \end{aligned} \quad (4.3)$$

Here, E_C is the charging energy of the dot and $\alpha_i = \frac{C_i}{C}$ is the “lever arm” of the i^{th} gate electrode. The energy required to add the N^{th} electron, termed as the addition energy, is given as:

$$E_{add}(N) = \mu_{N \leftrightarrow N+1} - \mu_{N-1 \leftrightarrow N} = E_C + \Delta E \quad (4.4)$$

This is the energy difference between ground-state electrochemical potentials. Here, $\Delta E = E_{N+1} - E_N$ is the energy difference between the consecutive electron states,

which can be zero in case electrons are added to the same spin-degenerate level. Excited states can also contribute to transport through the dot with associated electrochemical potentials:

$$\mu_{i \leftrightarrow j} = U_i(N) - U_j(N-1) \quad (4.5)$$

Here, i and j are used to index the states, with primes denoting excited states; for example, the electrochemical potential corresponding to the transition between the N electron ground state and the $N+1$ electron excited state is $\mu_{N \leftrightarrow (N+1)'}$.

4.2 Coulomb Spectroscopy

Transport through the quantum dot is possible if at least one chemical potential corresponding to a ground state N to ground state $N+1$ transition lies within the bias window, i.e., $\exists N$, such that $\mu_s \geq \mu_{N \leftrightarrow N+1} \geq \mu_d$, with the magnitude of current determined by the tunneling rates Γ_s and Γ_d . At the “Coulomb peaks”, the dot occupancy fluctuates between two or more charge occupancies, thus leading to a current. Otherwise, the dot is said to be Coulomb blockade, and the occupancy of the dot remains unchanged. For a fixed low source-drain bias ($eV_{sd}, k_B T \ll E_C$), this manifests as peaks in dot current at specific gate voltages. In the case of high source-drain bias, multiple electrochemical potential levels can participate in transport, allowing for transport via multiple parallel channels.

A 2D plot of dot current (or conductance) as a function of bias and gate voltages allows one to extract several parameters characterizing the quantum dot [fig 4.2]. The regions where the dot is in Coulomb blockade form the so-called Coulomb diamonds in the V_g - V_{sd} space. In the following discussion, the drain is assumed to be held at a constant zero potential ($V_d = 0 \Rightarrow \mu_s = -eV_{sd}$), which is the reference with respect to which all other voltages are applied. For low bias, i.e., $V_{sd} = 0$, current across the dot is non-zero when:

$$\mu_{N \leftrightarrow N+1} = E_{N+1} + E_C \left(N - N_0 + \frac{1}{2} \right) - \frac{E_C}{e} (C_g V_g) = \mu_s \quad (4.6)$$

This means that, as the gate voltage V_g is swept (keeping $V_{sd} = 0$), the current through the dot shows peaks separated by $\Delta V_g = e/C_g + \Delta E$, where $\Delta E = E_{N+1} - E_N$ if the peaks correspond to $\mu_{N \leftrightarrow N+1}$ and $\mu_{N-1 \leftrightarrow N}$.

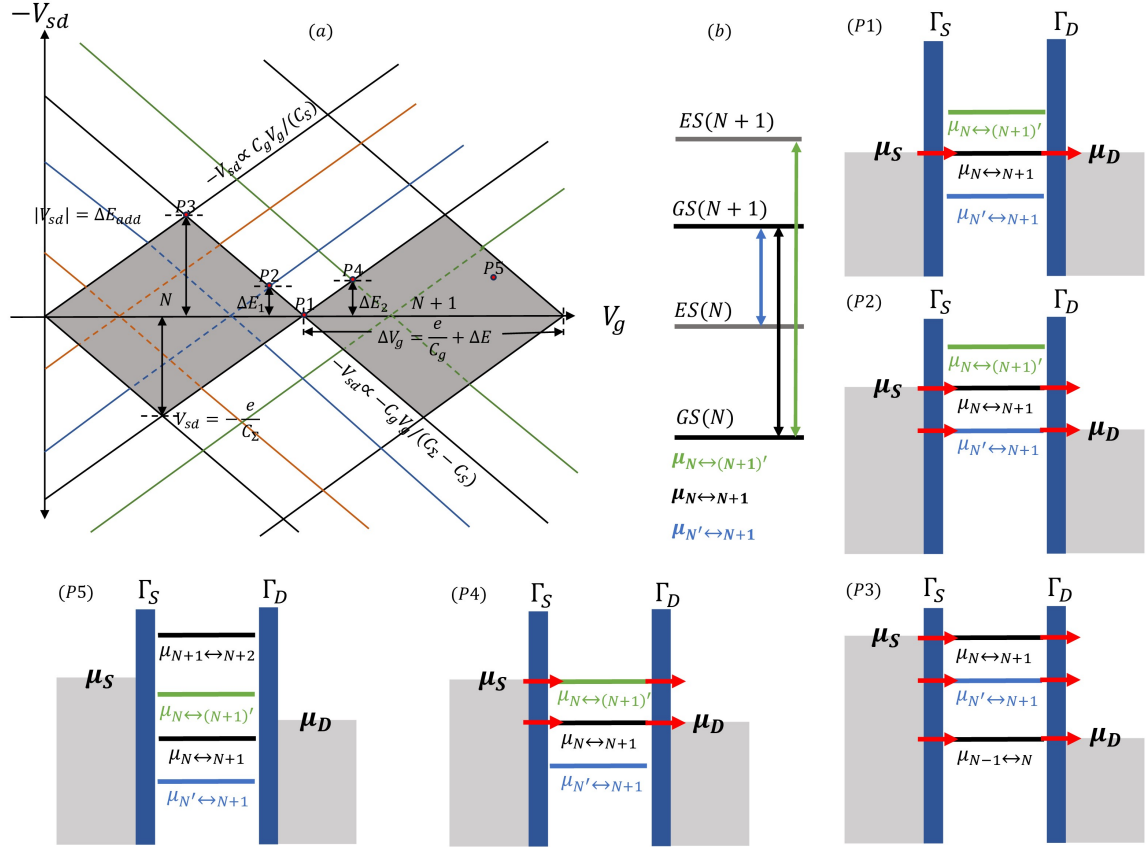


Figure 4.2: (a) A schematic of the quantum dot conductance as a function of the source-drain bias (V_{sd}) and plunger voltage (V_g). (P1) Low bias regime: transport through the dot occurs only when $\mu_{N \leftrightarrow N+1}$ aligns with μ_s and μ_d [7]. (P2), (P3), (P4), (P5) High bias regime: excited states may participate in transport, leading to higher current through the dot. The transitions involving excited states are allowed only when the respective electrochemical potential corresponding to the ground-to-ground state transition lies in the bias window. The dot is in “Coulomb blockade” (grey area) when none of the electrochemical potentials corresponding to ground state transitions between two dot occupancies lies in the bias window.

When the source chemical potential $\mu_s > \mu_d$ aligns with a level corresponding to a dot transition, say $\mu_{N \leftrightarrow N+1}$ then:

$$\mu_s = -eV_{sd} = E_{N+1} + E_C \left(N - N_0 + \frac{1}{2} \right) - \frac{E_C}{e} (C_g V_g + C_s V_{sd}) \quad (4.7)$$

$$\Rightarrow -V_{sd} = -\frac{C_g}{C_\Sigma - C_s} V_g + \lambda \quad (4.8)$$

Thus, in the $-V_{sd}$ vs V_g space, this is a straight line with slope $-C_g/(C_\Sigma - C_s)$. Similarly, the slope of the line corresponding to $\mu_d = 0 = \mu_{N-1 \leftrightarrow N}$ is C_g/C_s . Clearly,

lines corresponding to a new dot potential level aligning with one of the reservoirs will have the same slope as one of the two lines above, just different intercepts.

Point P3 in figure (4.2) corresponds to the $\mu_{N \leftrightarrow N+1}$ aligning with μ_s , and $\mu_{N-1 \leftrightarrow N}$ with μ_d . The source drain bias times the electronic charge ($|eV_{sd}|$) at P3 gives the addition energy $E_{add}(N) = \mu_{N \leftrightarrow N+1} - \mu_{N-1 \leftrightarrow N}$.

Excited state spectroscopy

Similarly, excitation energy can be calculated based on the bias voltage at certain intersections in the charge stability diagram. For instance, for the point P2 in figure (4.2) $\mu_{N \leftrightarrow N+1}$ is aligned with μ_s , and $\mu_{N' \leftrightarrow N+1}$ with μ_d , thus, $|eV_{sd}| = E_{N'} - E_N$.

In the absence of a magnetic field, any orbital state of the dot is two-fold spin degenerate, i.e., the state is equally likely to be filled with a spin-up \uparrow or a spin-down \downarrow electron. Contrary to this, if the magnetic field is switched on, this degeneracy is broken, and the charge transition lines in the charge stability diagram split into two. For example, the transition line joining P1, P2, and P3 in figure (4.2) would split in two. What was earlier $\mu_{N \leftrightarrow (N+1)}$ now splits to $\mu_{N \leftrightarrow (N+1)\downarrow}$ and $\mu_{N \leftrightarrow (N+1)\uparrow}$ differing in energy by $g\mu_B B$. In this case, the excitation energy ($\mu_{N \leftrightarrow (N+1)\uparrow} - \mu_{N \leftrightarrow (N+1)\downarrow} = \Delta E_z = g\mu_B B$) obtained from the Coulomb spectroscopy is field dependent. Most importantly, a measurement of ΔE_z vs magnetic field gives a straight line with slope $g\mu_B$, thus giving the material *g*-factor. In an exactly analogous manner, one can extract the field-dependent spin splitting, say, for example, in the singlet-triplet states for a dot occupancy of $N = 2$.

4.3 Charge Sensing

Direct transport measurement through quantum dots faces some fundamental problems. Firstly, it cannot be used to sense the charge state of dots not coupled to two reservoirs. This means it cannot be employed for measurements on an array of more than two dots. Another problem is that detecting measurable current across a dot needs the tunnel barriers to be below a certain value (for appreciable tunneling rates Γ_s and Γ_d). Because of the capacitive effect of the plunger gate on tunnel barriers, detecting currents below a certain dot occupancy may become a non-trivial task of

tuning gate voltages. This may be an issue when depleting down to the last electron.

Indirect charge sensing can be realized by using a quantum point contact (QPC) or a single electron transistor (SET) capacitively coupled to the quantum dot(s) whose charge state needs to be measured. A QPC can be used as a sensitive electrometer. In the case of QPCs, the sensor is tuned to a point of maximum slope at a transition between conductance plateaus. Here, the QPC conductance is most sensitive to changes in its electrostatic neighborhood. A SET is just a large quantum dot with smaller charging energy in comparison to the array dot [Orange dots shown in Fig. 2.4]. In the case of a SET, the SET dot’s electrochemical potential ladder is extremely sensitive to changes in the electrostatic profile near the dot. For instance, changes in charge occupancy of the coupled dot QD1 are seen as jumps/discontinuities in the CS current when tuned to a regime where Coulomb oscillations are observed. Due to the large contrast in signal at current peaks and regions of the blockade, very high contrast in the sensor signal is achievable over a large gate voltage space. In this regime, several charge transitions of QD1 can be observed by measuring current across CS without losing contrast [17].

4.4 Measurements on SQDs

4.4.1 Tuning a SQD

A semiconductor quantum dot is formed by electrostatically depleting the 2DEG in a quantum well. Here, we look at the tuning process for QD1, which extends to all other dots. The first step when “tuning” a quantum dot is to check the pinch-off curves of the backbone barrier gates [Fig. 4.3].

“Corner plots” (CPs) [Fig. 4.4] are recorded by measuring dot current (I_{SD}) while sweeping the barrier gates of the dot about their respective pinchoff values. This is done while keeping the plunger voltage constant. Discrete oscillations in current are seen at the corner of the non-zero current region before the current goes to 0 and the barriers completely pinch off. This region in the barrier space indicates the formation of a quantum dot with discrete energy states. The corner plots are repeated for dif-

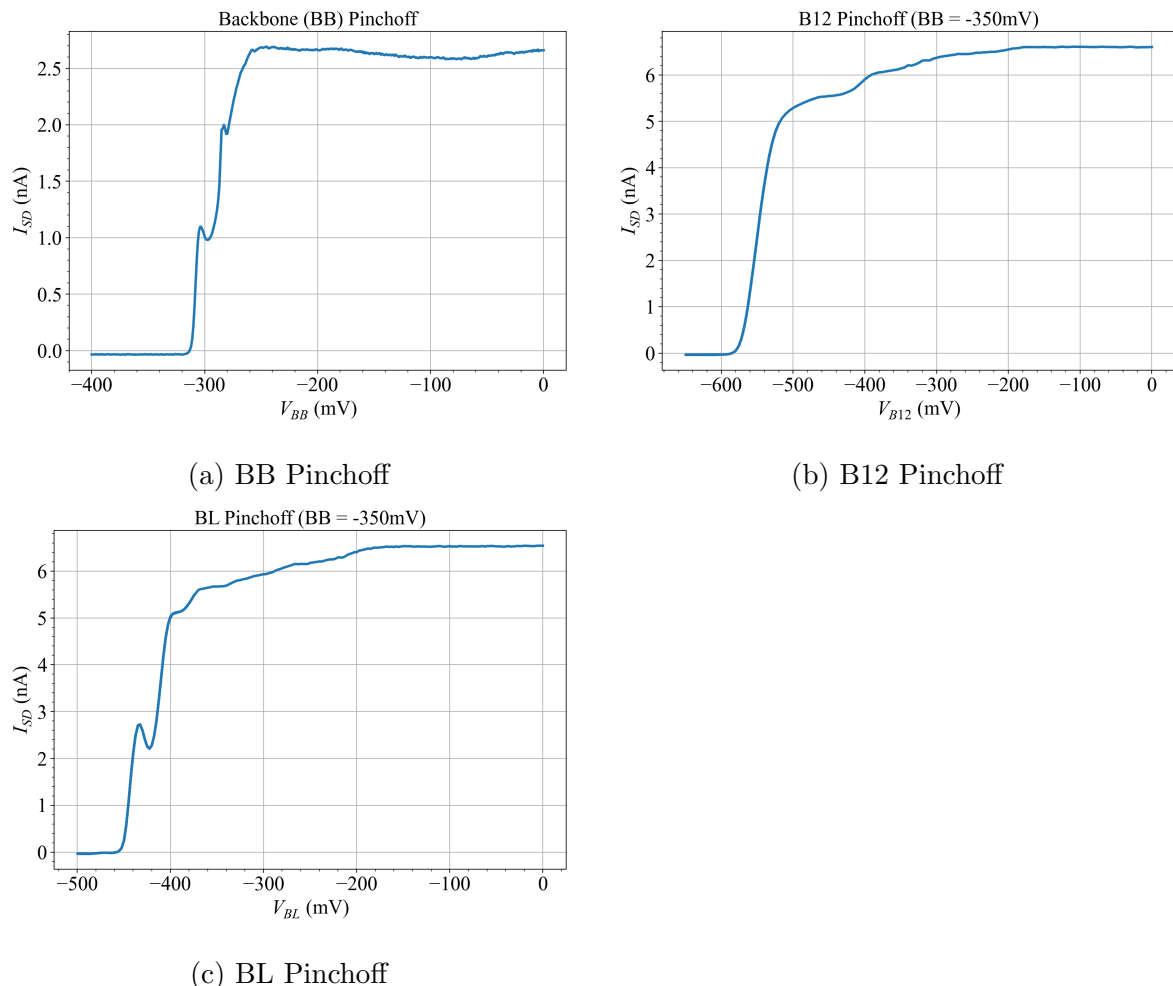


Figure 4.3: Pinchoff curves of the backbone and barriers of dot 1. The backbone is set at a constant value of -342mV (“completely pinched”) for all measurements reported.

ferent plunger voltages, and the one showing maximum fringes/oscillations in current is chosen to determine the barrier voltages.

Once the “optimal” barrier voltages are determined (these may be fine-tuned later), one can record Coulomb oscillations at low source-drain bias and move to Coulomb spectroscopy to fully characterize relevant dot parameters.

Quantum Dot 1

Fig. 4.5 shows the Coulomb diamond map recorded for QD1. The data is recorded using a Lock-In + DC conductance measurement. A $6\mu\text{V}$ AC signal at 245Hz is added to a DC bias, which is supplied to the source, while the drain goes to the input of the LIA for current measurement (indirect ground). $V_{BL} = -314\text{mV}$ and $V_{B12} = -517\text{mV}$

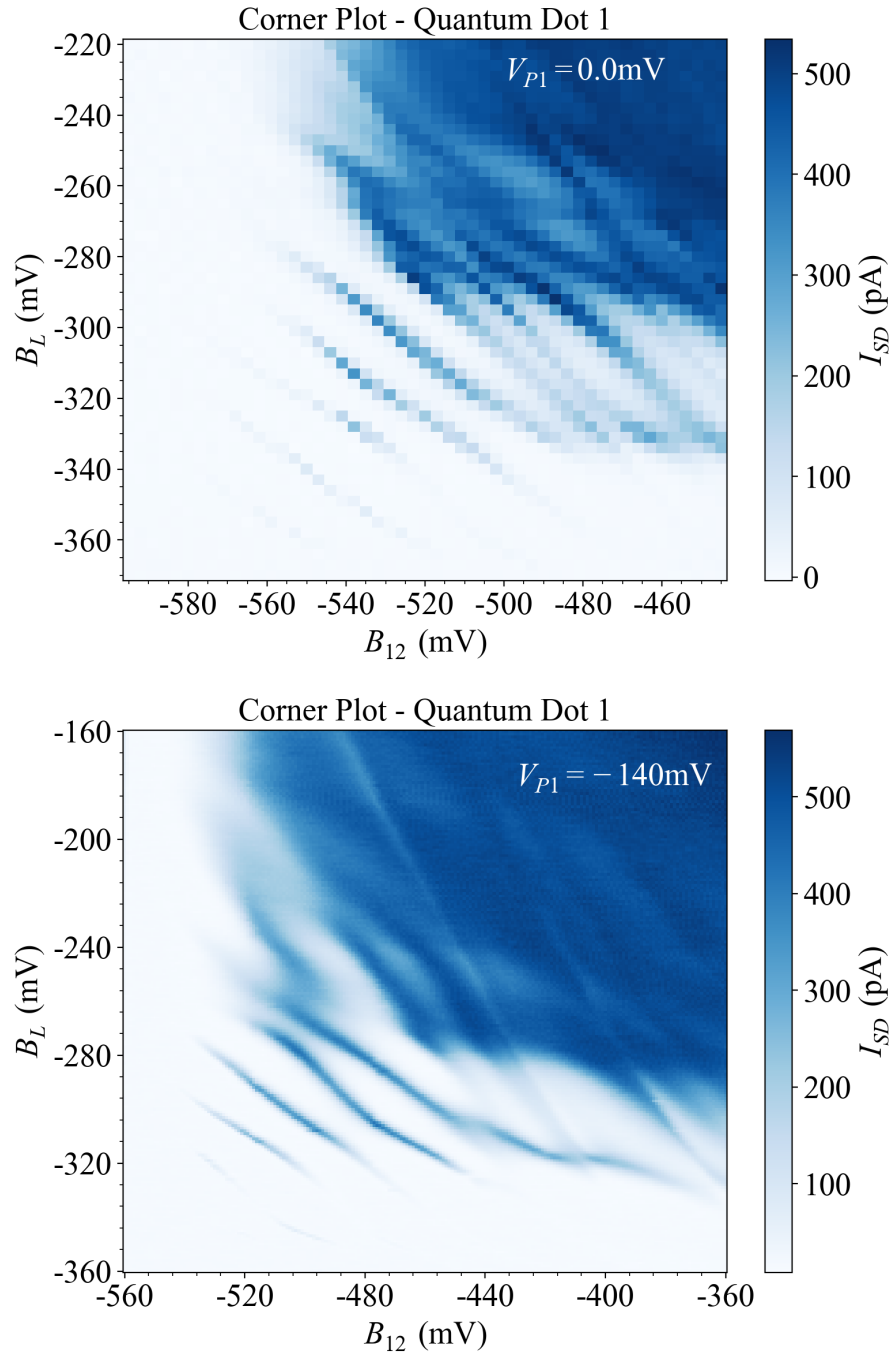


Figure 4.4: Corner plots for quantum dot 1. Plunger voltages are held constant during the sweeps (indicated on the plot). The oscillations in current are a signature of discretized energy states, and thus indicate the formation of a quantum dot.

are chosen from the corner plots [Fig. 4.4]. Following section 4.2, the dot lever arms come out to be $\alpha_{P1} = 0.088$, $\alpha_S = 0.175$, and $\alpha_D = 0.734$, while the charging energy for the N=3 is 1.861meV.

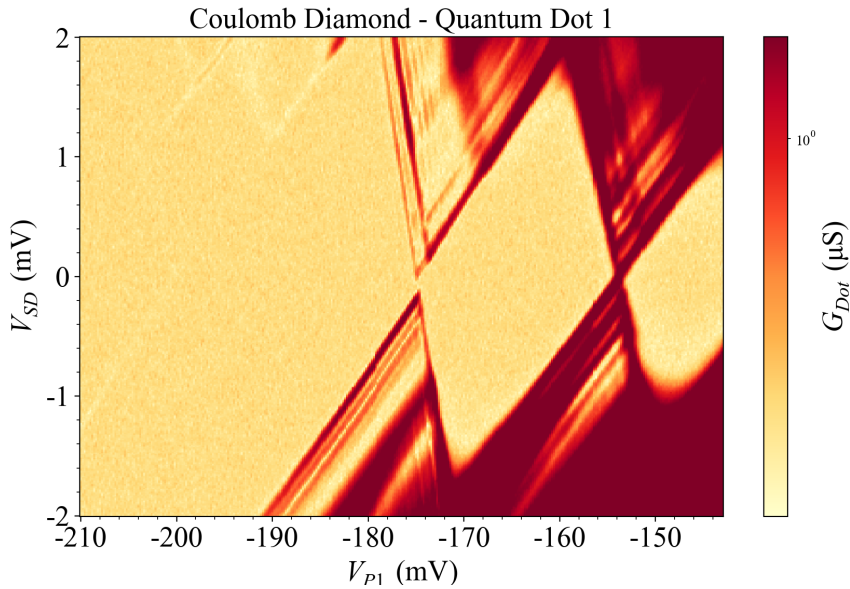


Figure 4.5: Coulomb diamonds for quantum dot 1. Using charge seeing along with transport, it is found that the last visible transition in transport corresponds to $N : 2 \leftrightarrow 3$

4.4.2 Electron Temperature

Measurements discussed in this work are conducted at a temperature of $\sim 10\text{mK}$. At such low temperatures, the electron-phonon coupling becomes weak (exact behavior is a material dependant). Thus, the lattice temperature, which is thermalized to the fridge, differs from the temperature of the 2DEG. The high-frequency electrical noise power dumped by the wires connecting the sample to hotter parts of the fridge and the currents sent through the ohmic cause the 2DEG to be at an elevated temperature compared to the lattice. This can be detrimental for qubit measurements. Thus, it is critical to determine the effective temperature of the electrons in the 2DEG before moving to qubit characterization. Finite electron temperature manifests as the thermal broadening of the Coulomb peaks along with effects due to lifetime broadening.

Consider transport through a really small channel (our quantum dot) coupled to two electron reservoirs with a small bias voltage applied: small enough that only a single electrochemical potential lies within the bias window [3]. A constant difference in the source-drain electrochemical potentials is maintained by an external voltage source: $\mu_s - \mu_d = -eV_{sd}$. If N electrons in steady state (net zero current flux $I_s = -I_d$)

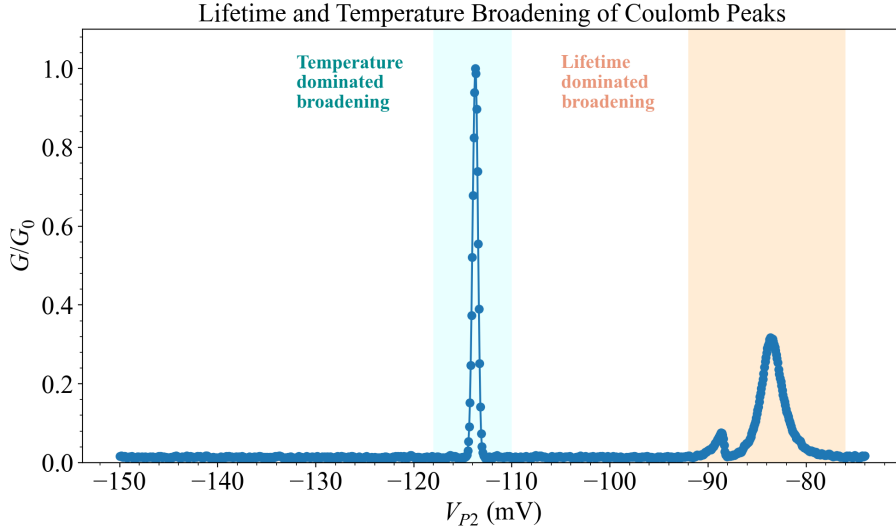


Figure 4.6: Peak broadening at different plunger voltages. For relatively transparent barriers ($\Gamma\hbar > k_B T$), the peak profile resembles a Lorentzian, while for opaque barriers ($\Gamma\hbar \ll k_B T$), the peak profile resembles a \cosh^{-2} [Eqn. 4.15].

occupy the dot, and $f_s(\mu) = f_{FD}(\mu - \mu_s)$ and $f_d(\mu) = f_{FD}(\mu - \mu_d)$ are the reservoir Fermi functions, then the current fluxes through each contact are:

$$I_s = e\Gamma_s(f_s - N), \quad I_d = e\Gamma_d(f_d - N) \quad (4.9)$$

$$N = \frac{\Gamma_s f_s + \Gamma_d f_d}{\Gamma_s + \Gamma_d} \quad (4.10)$$

$$I = I_s = -I_d = e \frac{\Gamma_s \Gamma_d}{\Gamma_s + \Gamma_d} (f_s - f_d) \quad (4.11)$$

The tunneling rates Γ_s and Γ_d give the rate at which an electron tunnels into the dot from the source or out to the drain from the dot, respectively. No current flows when a level μ is much above (below) both μ_s and μ_d since $f_s(\mu) = f_d(\mu) = 0$ ($f_s(\mu) = f_d(\mu) = 1$). Transport through the dot is only possible if μ lies within a few $k_B T$ of μ_s and μ_d , i.e., when $\mu_s > \mu > \mu_d$. For symmetric tunneling rates $\Gamma = 2\Gamma_s = 2\Gamma_d$, the current value at the Coulomb peak ($\mu_s > \mu > \mu_d$, thus $f_s \simeq 1$ and $f_d \simeq 0$) allows one to experimentally extract Γ . For gate-defined quantum dots, Γ is highly tunable using barrier gate voltages. Coupling of the dot with the reservoirs leads to a finite lifetime of the electron in the dot ($\tau \sim \Gamma^{-1}$). This can be seen as a broadening of the Coulomb peak due to the DOS in the dot spreading out around μ . In the simplest case, this is a Lorentzian about $E = \mu$:

$$D_\mu(E) = \frac{1}{\pi} \frac{\Gamma\hbar/2}{(E - \mu)^2 + (\Gamma\hbar/2)^2} \quad (4.12)$$

Here, $\Gamma = \Gamma_s + \Gamma_d$. The corresponding current and dot occupation are:

$$I = e \int_{\mu_d}^{\mu_s} dE D_\mu(E) \frac{\Gamma_s \Gamma_d}{\Gamma_s + \Gamma_d} (f_s - f_d) \quad (4.13)$$

$$N = \int_{-\infty}^{+\infty} dE D_\mu(E) \frac{\Gamma_s f_s + \Gamma_d f_d}{\Gamma_s + \Gamma_d} \quad (4.14)$$

For small bias and low temperatures $f_s(E) - f_d(E) \simeq 1$ iff $\mu_s > E > \mu_d$, else 0. So, the current profile of the Coulomb peak is a Lorentzian with FWHM = $(\Gamma_s + \Gamma_d)\hbar$ instead of a sharply peaked delta function along $e\alpha_P V_P$ axis.

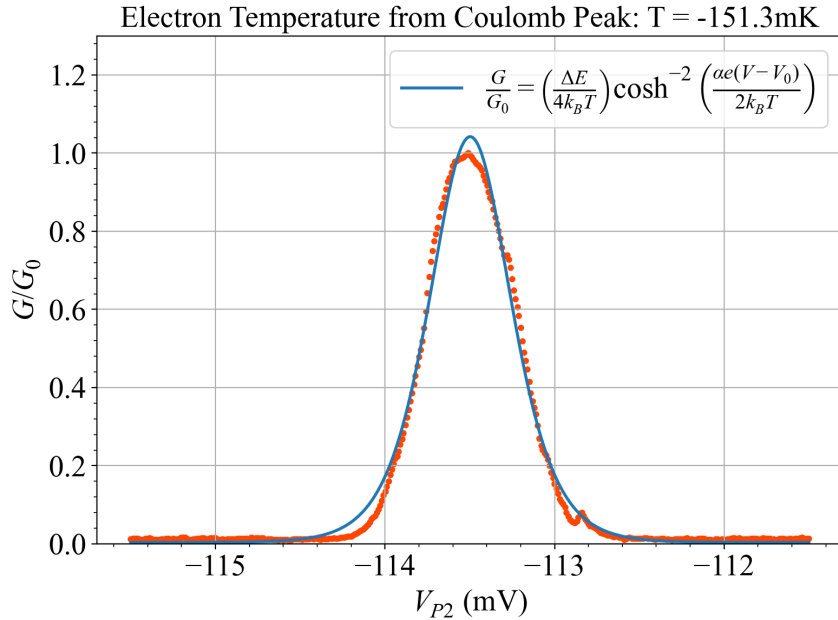


Figure 4.7: Conductance peak fitting for electron temperature extraction. This is the regime where thermal broadening is dominant and $\Gamma\hbar \ll k_B T$ [left peak in Fig. 4.6].

However, broadening of Coulomb peaks is caused by two effects [Fig. 4.6]: broadening of the dot level associated with the finite lifetime of the electron in the dot and the Fermi distribution of the reservoirs at finite temperature ($f_{FD}(E - \mu_{res}, T_{res})$). For sufficiently opaque barriers, in the quantum regime: $\Gamma\hbar \ll k_B T \ll \Delta E_C$. In this case, the profile of the conductance peak allows for the extraction of the electron temperature as [2],[19]:

$$\frac{G}{G_0} = \left(\frac{\Delta E}{4k_B T} \right) \cosh^{-2} \left(\frac{\alpha e(V - V_0)}{k_B T} \right) \quad (4.15)$$

Here, $\alpha_{P2} = 0.083$ is obtained from the Coulomb diamond map for QD2 [Fig. 4.8]. Fitting equation 4.15 [Fig.4.7], the electron temperature is estimated to be 151.3mK.

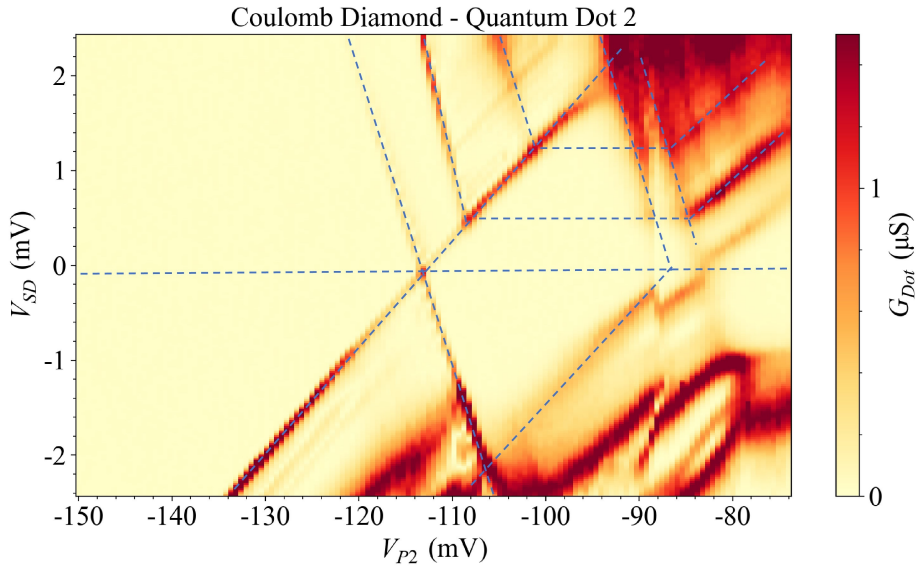


Figure 4.8: Coulomb diamonds for quantum dot 2. The slopes of the sides of the diamond give the gate and reservoir lever arms, whilst the size of the diamond gives the addition energy for the particular transition [Fig. 4.2].

The electron temperature for the initial cooldown of the sample was measured to be around 300mK. During this run, half of the gates and two ohmics were unfiltered, whereas others were filtered using an RC+RF Q-filter combination. During the final cooldown, another set of filters was added, with all lines now having an RC + RF filter with 62.5kHz and 1.2MHz cutoff frequencies, respectively.

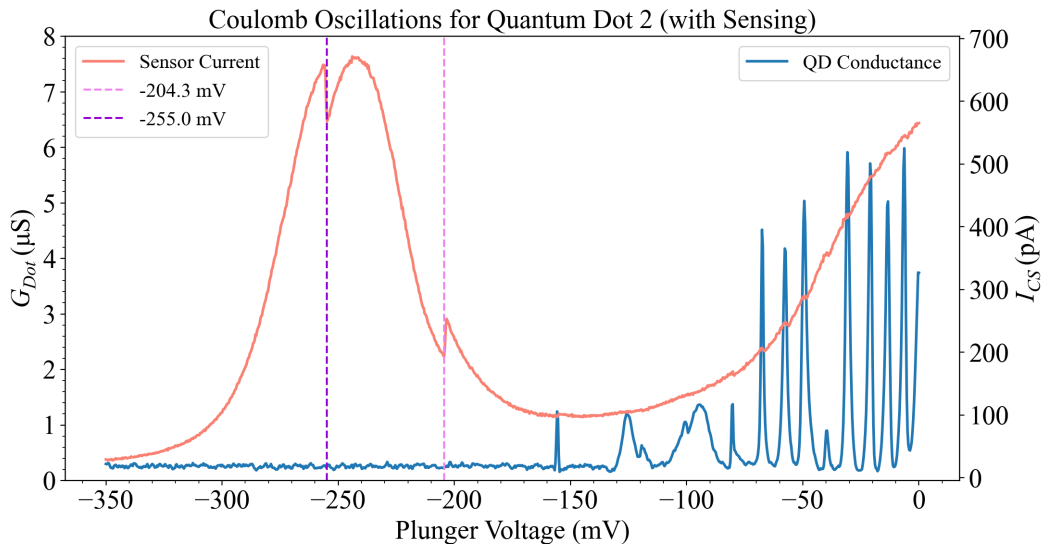


Figure 4.9: Coulomb oscillations for quantum dot 2 - sensing + transport. Discrete jumps in the charge sensor signal indicate a change in occupancy of QD2.

4.4.3 Going down to the Last Electron

Charge sensing measurements indicate that current/conductance peaks in transport are only seen down to the $N : 2 \leftrightarrow 3$ for most dots in the array [Fig. 4.9] due to “pinching off” of the tunnel barriers when sweeping the plunger. The decrease in tunneling rates with increasing negative voltage on the plunger gate is a consequence of the non-zero cross-talk of the plunger gate with the tunnel barriers. The extent of the effect is strongly dependent on the lithographic features of the device.

Chapter 5

Double Quantum Dots

5.1 Constant Interaction Model

Lateral double quantum dots can be modeled as two conducting puddles of a finite number of electrons, tunnel coupled with one another, capacitively coupled to gate electrodes, and tunnel coupled with one reservoir on either side. Analogous to the

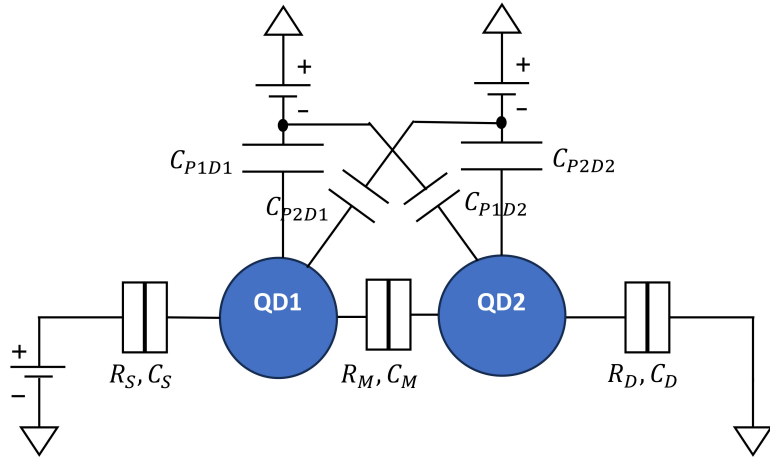


Figure 5.1: A schematic circuit model of a Double Quantum Dot with cross capacitances considered.

discussion in section 4.1, the charge on each dot can be written as:

$$Q_1 = C_{P1D1}(V_1 - V_{P1}) + C_{P2D1}(V_1 - V_{P2}) + C_M(V_1 - V_2) + C_S(V_1 - V_S) \quad (5.1)$$

$$Q_2 = C_{P2D2}(V_2 - V_{P2}) + C_{P1D2}(V_2 - V_{P1}) + C_M(V_2 - V_1) + C_S(V_2 - V_S) \quad (5.2)$$

Here, one can solve for V_1 and V_2 given $Q_1 = -eN_1$ and $Q_2 = -2N_2$.

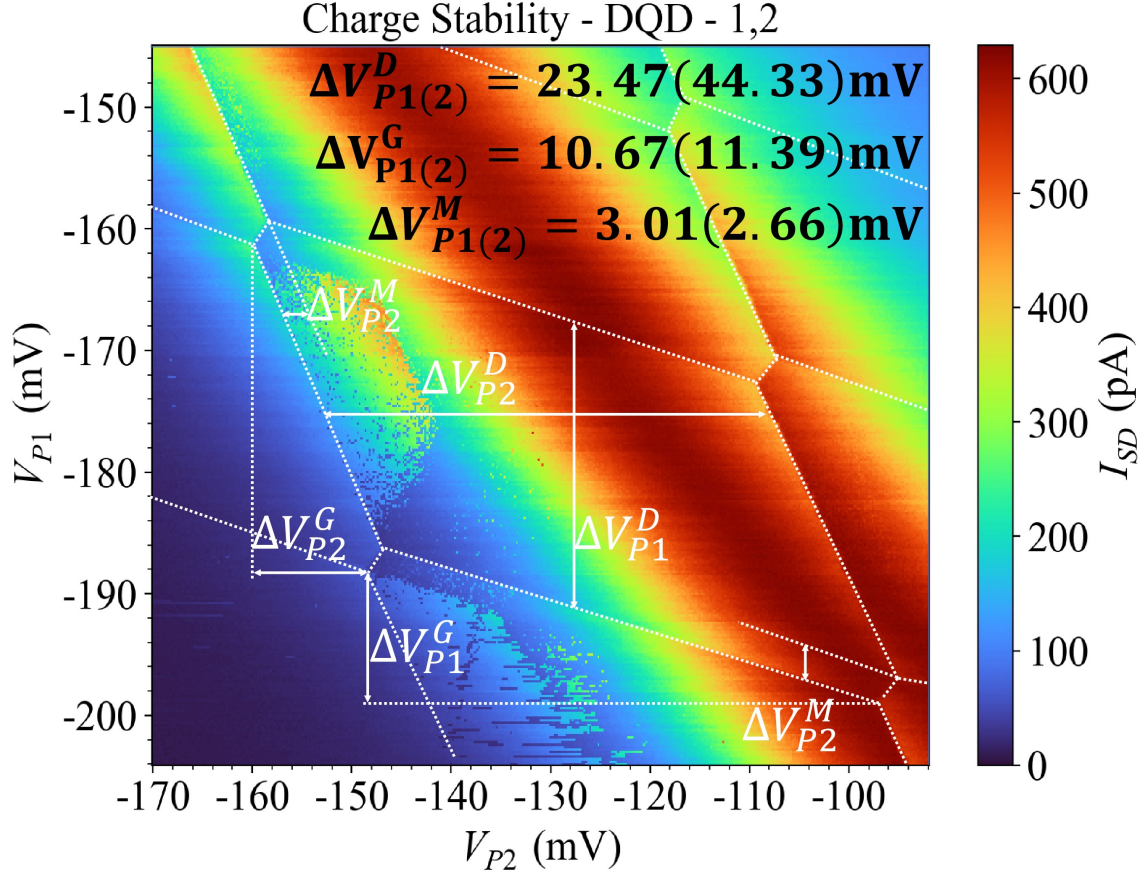


Figure 5.2: Measured charge stability diagram of DQD 1,2 using sensing. Different parameters of the hexagon (in gate space) allow for the estimation of the double dot capacitances.

If the cross capacitances C_{PiDj} ($i \neq j$) are neglected (or virtual gates are used to compensate for this effect), it can be shown that the electrostatic contribution of the dot energy is [14]:

$$U(N_1, N_2) = \frac{1}{2}N_1^2 E_{C1} + \frac{1}{2}N_2^2 E_{C2} + N_1 N_2 E_{CM} + f(V_{P1}, V_{P2}) \quad (5.3)$$

Where the first two terms are the energy terms due to the Coulomb repulsion of electrons within each dot, and the third term is the inter-dot Coulomb repulsion. The fourth term is the induced charges due to capacitances with gates:

$$\begin{aligned} f(V_{P1}, V_{P2}) = & -\frac{1}{e} C_{P1} V_{G1} (N_1 E_{C1} + N_2 E_{CM}) + C_{P2} V_{G2} (N_2 E_{C2} + N_1 E_{CM}) \\ & + \frac{1}{e^2} \left\{ \frac{1}{2} C_{G1}^2 V_{G1}^2 E_{C1} + \frac{1}{2} C_{G2}^2 V_{G2}^2 E_{C2} + C_{G1} V_{G1} C_{G2} V_{G2} E_{CM} \right\} \end{aligned}$$

Here, $E_{C1} = e^2 C_2 / C^2$, $E_{C2} = e^2 C_1 / C^2$, and $E_{C1} = e^2 C_M / C^2$, where $C^2 = C_1 C_2 - C_M^2$ and $C_{1(2)} = C_{S(D)} + C_{G1(2)} + C_M$.

Similar to the single dot case, the electrochemical potential for a particular transition is defined as:

$$\mu_1(N_1, N_2) = U(N_1, N_2) - U(N_1 - 1, N_2) \quad (5.4)$$

$$\mu_2(N_1, N_2) = U(N_1, N_2) - U(N_1, N_2 - 1) \quad (5.5)$$

Using the above equations for zero bias case for the system in figure 5.1[17][27]:

$$C_{P1(2)D1(2)} = \frac{e\Delta V_{G2(1)}^D}{\Delta V_{G1}^D \Delta V_{G2}^D - \Delta V_{G1}^G \Delta V_{G2}^G} \quad (5.6)$$

$$C_{P1(2)D1(2)} = \frac{e\Delta V_{G2(1)}^G}{\Delta V_{G1}^D \Delta V_{G2}^D - \Delta V_{G1}^G \Delta V_{G2}^G} \quad (5.7)$$

$$\frac{C_{1(2)}}{C_M} = \frac{e}{C_{G2(1)D2(1)} \Delta V_{G2(1)}^M} - \frac{C_{G2(1)D1(2)}}{C_{G2(1)D2(1)}} \quad (5.8)$$

For the DQD-1,2, the values obtained are: $C_{P1D1}=7.72\text{aF}$, $C_{P2D2}=4.09\text{aF}$, $C_{P1D2}=1.98\text{aF}$, and $C_{P2D1}=1.86\text{aF}$.

5.2 Measurements on DQDs

5.2.1 Tuning a DQD

The initial steps involved in tuning a DQD are similar to those for a SQD. First, a large single dot is formed by “pinching” outer barriers, say, BL and B23, while keeping B12, P1, and P2 transparent. Initial BL and B23 values are chosen in the region of the corner plot where the current is non-zero but falling. Next, plunger maps are recorded by sweeping V_{P1} and V_{P2} while keeping barriers fixed. Slowly, the middle barrier is pinched, taking the system from $C_M \sim C_{1(2)}$ to $C_M < C_{1(2)}$. This is equivalent to splitting the large dot formed earlier into smaller coupled quantum dots [Fig. 5.3].

Once the DQD is tuned using transport, charge sensing is used to go to more negative plunger voltages in order to reach (0,0) charge occupancy.

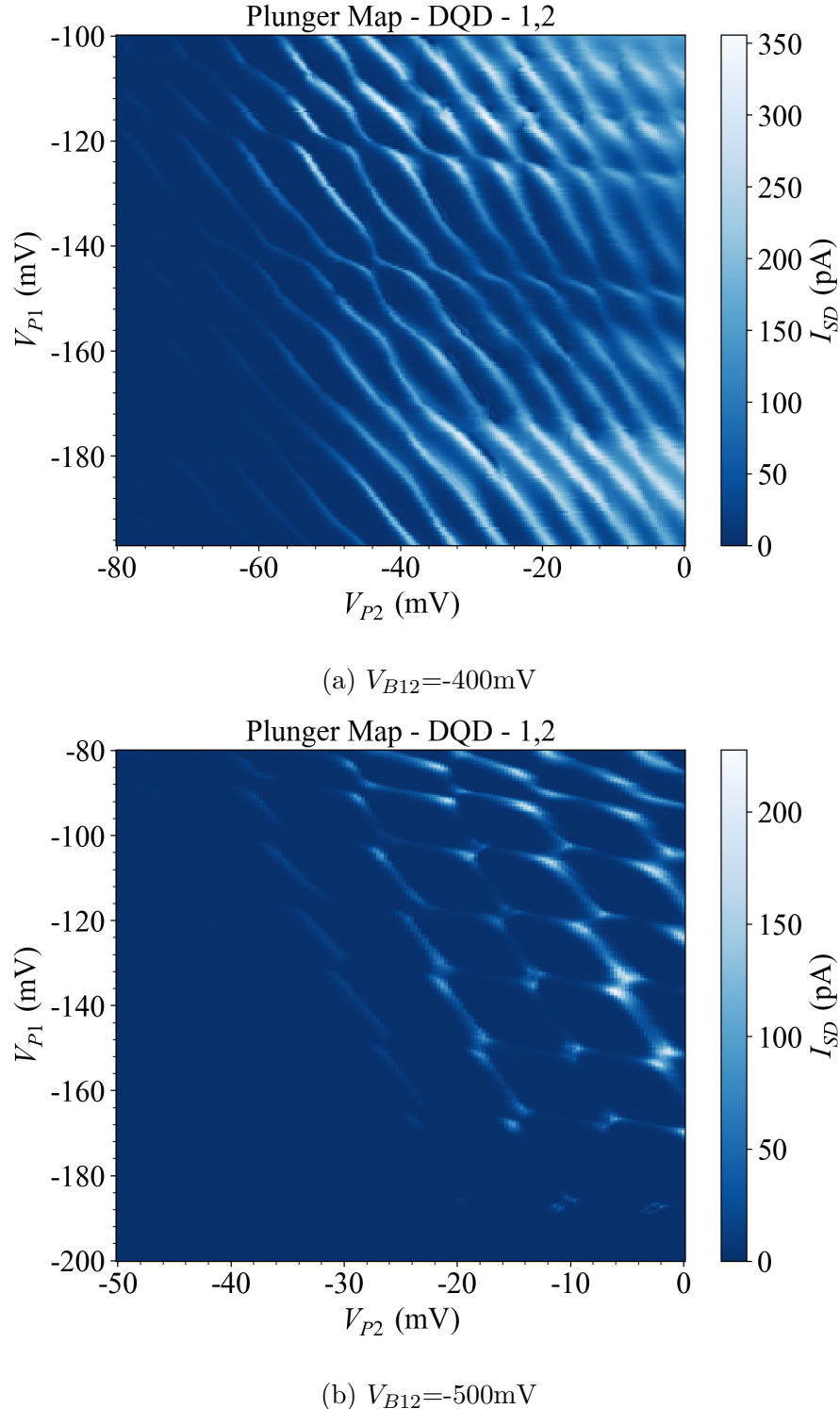


Figure 5.3: Plunger maps for different middle barrier (V_{B12}) voltages. Plot (a) is a regime where $C_M \ll C_{1(2)}$, and the system resembles a large SQD or a very strongly coupled DQD. Plot (b) is a regime where $C_M \sim C_{1(2)}$ which shows the formation of the characteristic hexagonal charge stability diagram for the DQD system. Here, triple points with high current are joined by sides of the hexagon where current is predominantly due to cotunneling.

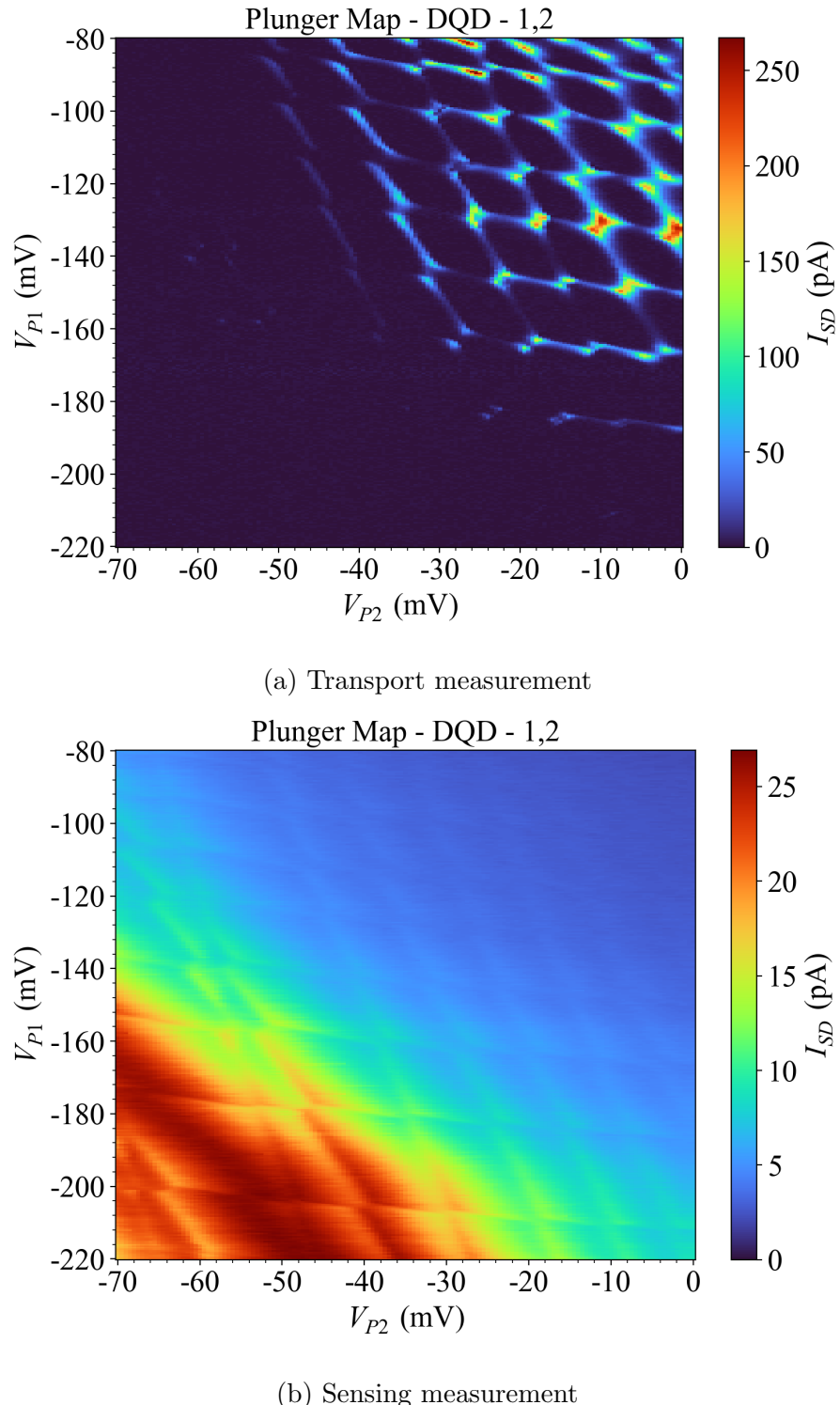


Figure 5.4: Plunger maps for identical barrier gate voltages in transport and sensing. Sensing allows for the detection of charge state much beyond the plunger space when the transport signal is visible.

Chapter 6

Spin Readout and T_1 measurement

6.1 Elzerman Spin readout (ERO)

Realizing high-fidelity readout of the qubit state [Criterion 5, section 1.2] in the case of spin qubits translates to the high-fidelity measurement of the spin state. Indirect measurement of the spin state is done using spin-to-charge conversion. Elzerman pin readout (ERO) [5] is one such scheme. ERO uses a four-step pulse sequence to read out the spin state based on different electrical responses for the two spin states owing to selective tunneling possible for the \downarrow spin state in the read-out part of the sequence.

6.1.1 T_1 Measurement using ERO

A pulse scheme very similar to the one described in figure (6.1) can be used to measure T_1 , the relaxation time constant for the higher energy spin-down \downarrow state of the electron in a dot [23].

The first step loads an electron into the excited state with a certain probability p_0 , or into the ground state with probability $(1 - p_0)$ which can be determined. This is followed by waiting at the same voltage, during which if the electron is in the excited state and survives the wait-time without decaying to the ground state, a jump in signal is seen in the read-out pulse when \downarrow tunnels out, and a \uparrow is loaded. The third step unloads \uparrow to empty the dot. Measurements of the signal over several such pulse sequences are averaged to get a signal. The average value of the jump in the read-out part is measured for different wait times. With increasing wait-time t_{wait} , the fraction

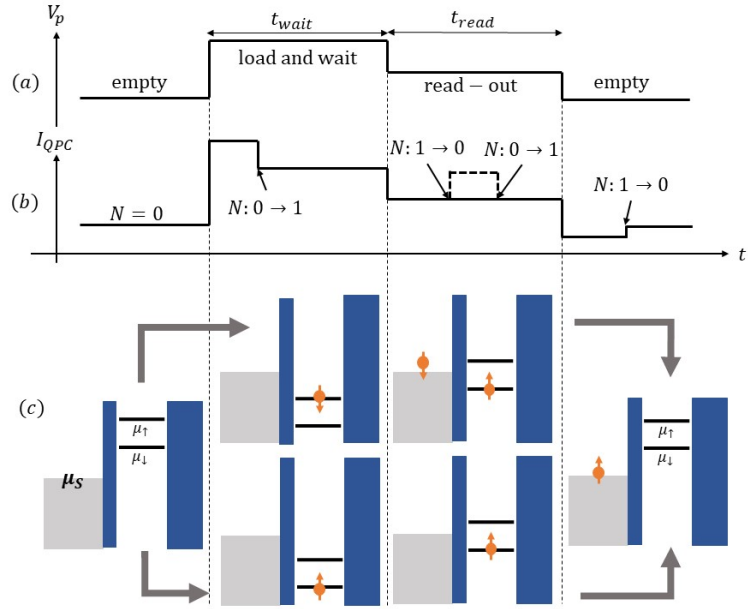


Figure 6.1: Schematic for ERO (a) Pulse sequence applied to the quantum dot plunger gate to raise/lower the electrochemical potential ladder. (b) Response of a QPC charge sensor: responds to charge jumps as well as plunger voltage changes. The signal obtained in case a spin-up electron (dotted) is loaded shows an added jump in the read-out step. This jump is seen when the spin-down electron tunnels out and a spin-up electron is filled. (c) Schematic of the dot configuration.

of instances when a jump is seen during the read interval will decay exponentially as $p = p_0 e^{-t_{wait}/T_1}$ (assuming that the $T_1 \gg 1/\Gamma$, Γ being the tunneling rate to the lead). The jump signal average vs t_{wait} , shows an exponential decay with a time constant equal to the spin-lattice relaxation time T_1 .

6.2 Pauli Spin Blockade

Schemes like the ERO and tunneling rate dependent spin readout [8] rely on the tunneling of the spin out of the dot into the reservoirs. Thus, such schemes are not extendible to an array, where there might be one or more dots that may not be directly coupled to a lead/reservoir. Pauli spin blockade (PSB) [15][12] based spin readout can be used to circumvent these issues. Here, a double quantum dot system is used to read out the spin state of a spin in, say, QD1 with a spin (electron) in QD2 by exploiting the delayed relaxation of the separated spin-triplet state to a singlet due to Pauli's exclusion principle.

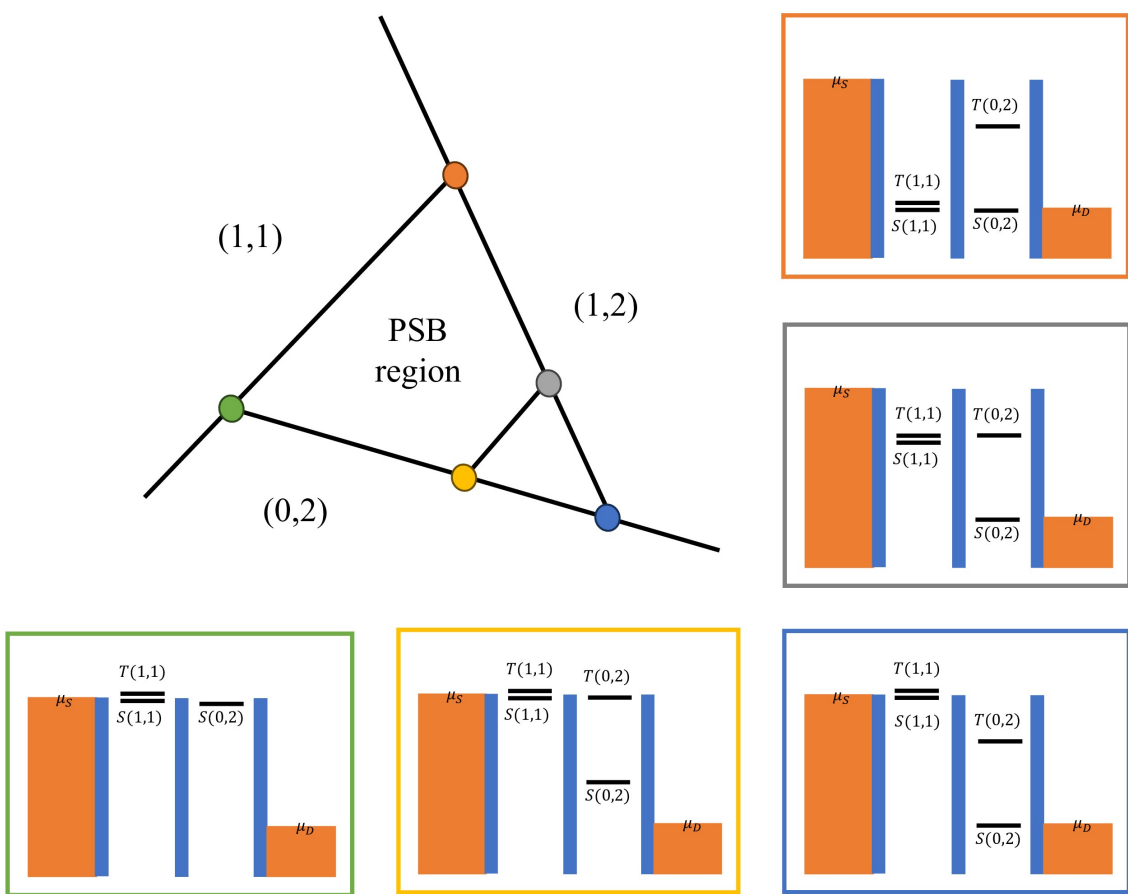


Figure 6.2: Blockade in “reverse bias”

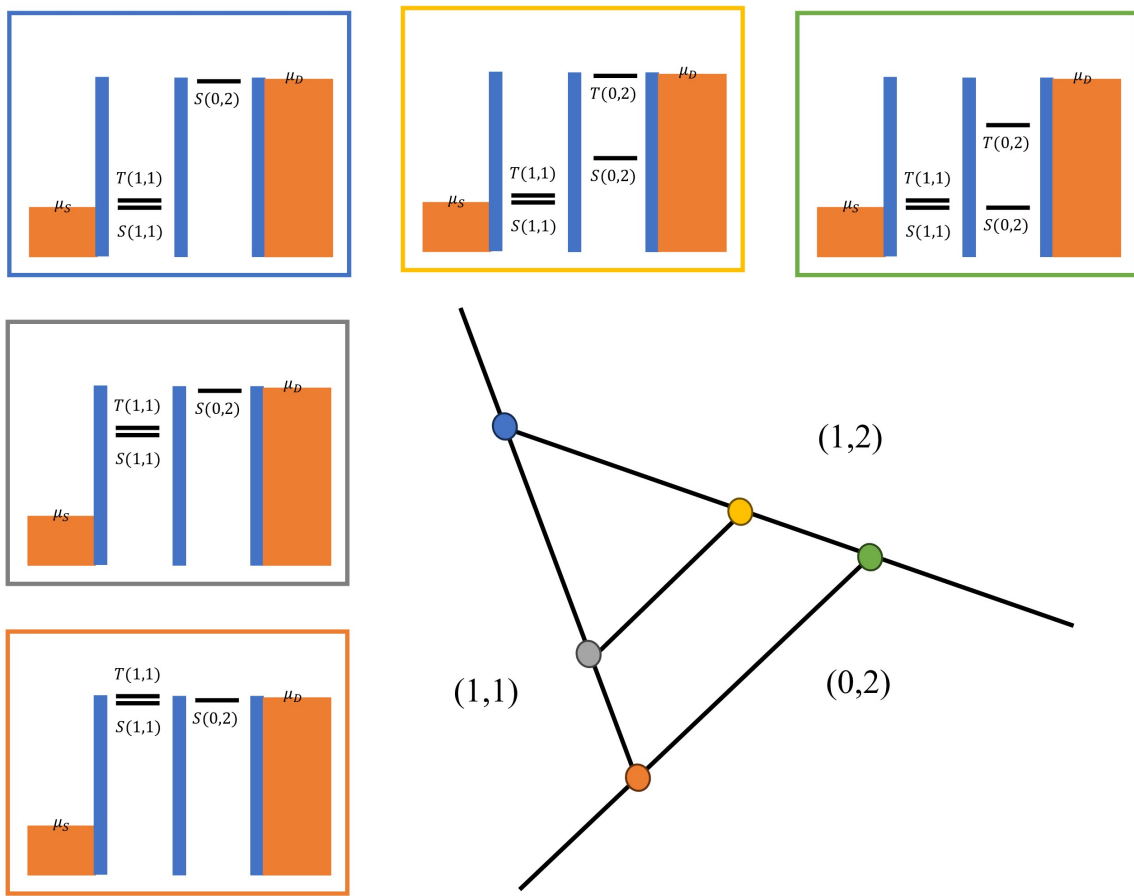


Figure 6.3: Blockade in “forward bias”

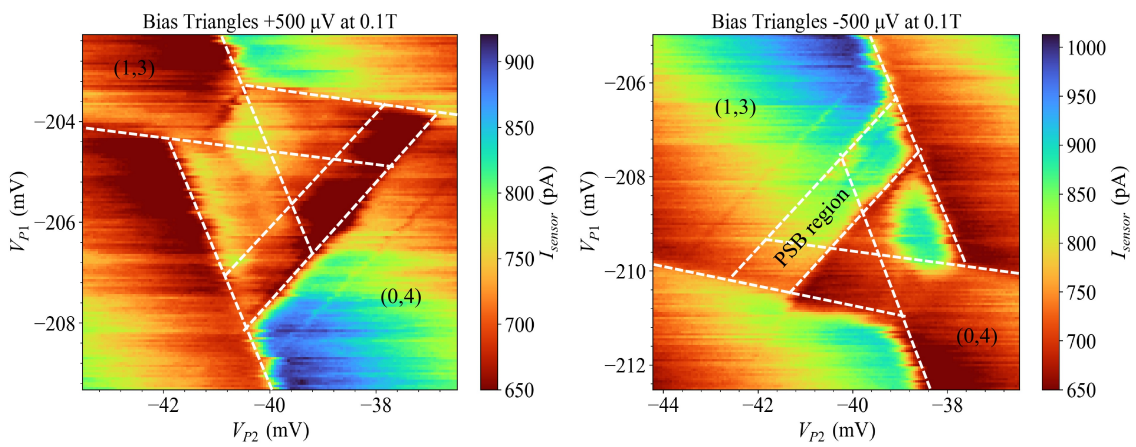


Figure 6.4: Pauli Spin Blockade (PSB) at the (1,3) to (0,4) charge transition

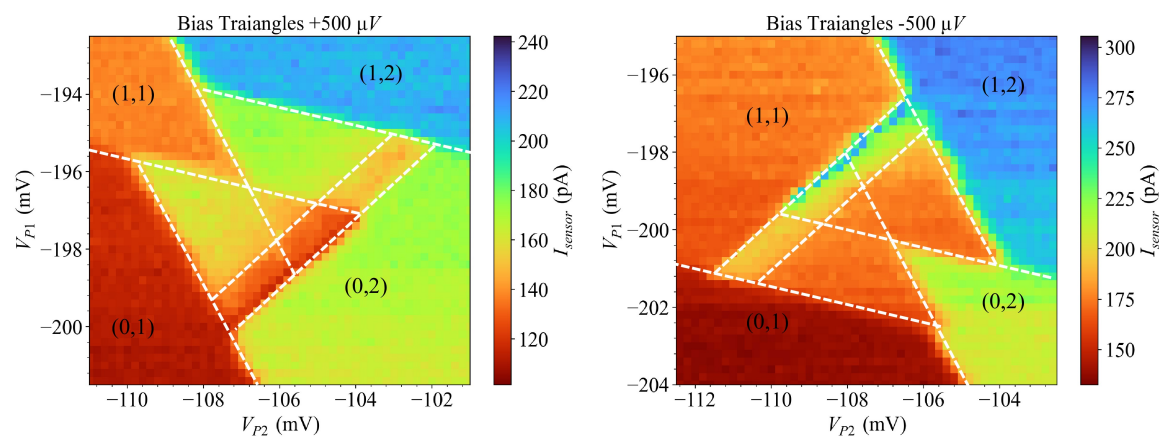


Figure 6.5: Blockade lifted (PSB) at the (1,1) to (0,2) charge transition.

Chapter 7

Experimental Setup

7.1 Dilution Fridge

7.1.1 Working Principle [1]

All practically realized quantum processors rely on the qubits being cooled to cryogenic temperatures much below liquid nitrogen temperatures using several cooling techniques. Simply put, the thermal energy $k_B T$ must be much smaller than the energy difference of eigenstates of your two-level quantum system to be able to demonstrate any quantum operations. Coherent control of spin qubits has been demonstrated at temperatures as “high” as 4K ([10], [21]). Thus, the field of quantum computing has heavily relied on advances in the field of cryogenics. All measurements discussed in the thesis were carried out in a Bluefors LD-400 dry dilution refrigerator (DR) with a base temperature of 10mK. Understanding the workings of, setting up, and using a dilution refrigerator was a critical part of my project, and this section gives an overview of the same.

Joule-Thomson cooling is a phenomenon where the temperature of a gas drops due to sudden (nearly) isenthalpic expansion, often after being forced through a small constriction at high pressures. JT expansion, cooling by expansion/pumping, and evaporative cooling are commonly used in refrigeration and cryogenics. Pumping on a liquid coolant can be used to achieve temperatures lower than its normal boiling point using evaporative cooling; for instance, liquid ^4He (boiling point 4.2K at 1 atm) can be used to achieve temperatures down to 1.2K, while pumping on liquid ^3He

(boiling point 3.19K at 1 atm) can be used to go down to $\sim 250\text{mK}$ owing to the higher vapor pressure of ${}^3\text{He}$. Reaching temperatures as low as $\sim 10\text{mK}$ requires the so-called “dilution process.”

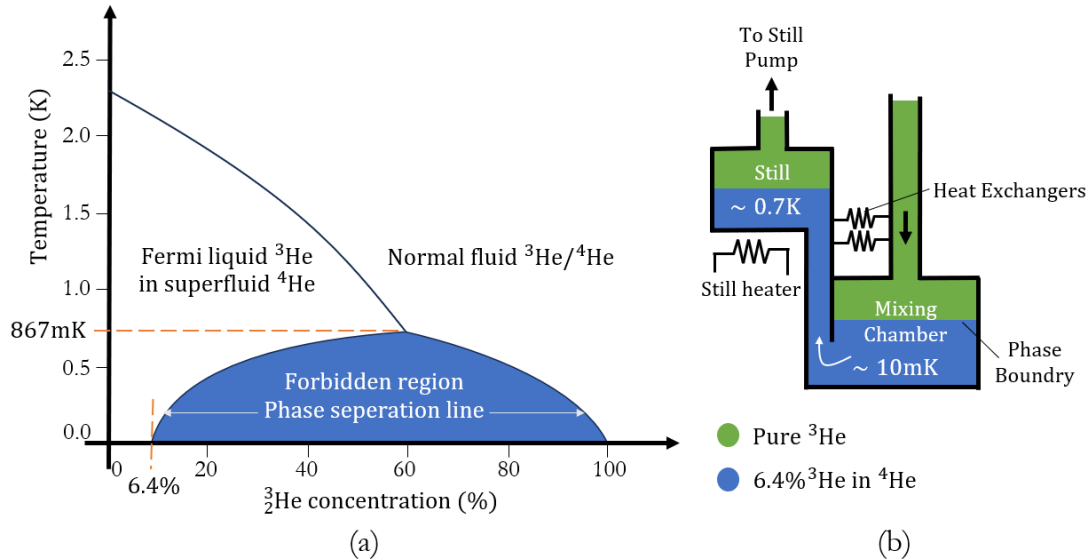


Figure 7.1: (a) Phase diagram for ${}^3\text{He}$ - ${}^4\text{He}$ mixing. (b) Schematic showing the key sections of a dilution refrigerator.

${}^4\text{He}$ obeys Bosonic statistics and undergoes a transition to a superfluid state at 2.17K, whereas ${}^3\text{He}$ obeys Fermi statistics and it becomes superfluid below 1mK. Below 870mK, the ${}^3\text{He}$ - ${}^4\text{He}$ mixture undergoes a phase separation into a pure liquid ${}^3\text{He}$ phase and a dilute phase of ${}^3\text{He}$ in superfluid ${}^4\text{He}$. The working of dilution refrigerators relies on the finite solubility of ${}^3\text{He}$ in superfluid ${}^4\text{He}$ down to 0K due to the higher Van der Waals attraction between ${}^3\text{He}$ - ${}^4\text{He}$ than ${}^3\text{He}$ - ${}^3\text{He}$. If ${}^3\text{He}$ atoms are removed from the diluted phase [Fig. 7.1], ${}^3\text{He}$ atoms from the concentrated phase cross the phase boundary to occupy the vacant energy states, absorbing energy, thus, providing the cooling at the Mixing Chamber (MXC). The constant ${}^3\text{He}$ vaporization to the gaseous phase takes place at the Still chamber where external pumping and heating maintain a sufficient rate of vaporization of ${}^3\text{He}$, thus sustaining the dilution cycle. ${}^4\text{He}$ has much lower vapor pressure compared to ${}^3\text{He}$ at the Still temperature, which is key for selectively maintaining a constant flow of ${}^3\text{He}$ across the phase boundary at the MXC. Thus, the resulting cooling power at MXC is the flow rate (\dot{n}) multiplied by the associated enthalpy difference due to dilution (ΔH): $\dot{Q} = \dot{n}\Delta H \propto \dot{n}T^2$. Modern DRs use a pulse tube refrigerator (PTR) to pre-cool the

DR to about 3K. It contains an intermediate Joule-Thomson stage, where ^3He passes through a high impedance constriction, which cools it enough to liquify the ^3He on its way to the dilution unit (DU). The ^3He is cooled further before entering the MXC by a series of heat exchangers that thermalize it with various stages ^3He between the Still and the MXC [Fig. 7.1].

7.1.2 Setup

The DR consists of four consecutive stages, each at a lower temperature than the one above during operation, with the MXC being the last plate, reaching temperatures down to 10mK. Initially, the 4K, Still, and MXC plates are thermalized using heat switches. The 4K plate is thermalized to the pulse tube (PT), which provides the cooling power to pre-cool the system to low enough temperatures to start the dilution cycle. This also cools the NbTi magnet down to $\sim 2.7\text{K}$. Upon reaching temperatures low enough to start the dilution process, the heat switches are “turned off” (exchange gas in the chambers is absorbed by cooling down charcoal traps). This thermally isolates the plates below 4K, which are cooled to lower temperatures when the ^3He - ^4He mixture is circulated. The Still chamber is heated and is pumped on by a molecular turbo pump backed by a scroll pump to sustain the ^3He flow rate. The 4K, Still plate, Cold plate, and the MXC plate are typically at $2.6 - 3\text{K}$, $\sim 800\text{mK}$, 500mK , and 10mK during normal operation.

The sample is mounted on a cold finger suspended on the MXC plate. The significant thermal mass of the cold finger and RF filter setup means that the temperature of the sample mounted at the bottom of the cold finger differs slightly from the MXC temperature, thus requiring dedicated sensors mounted close to the sample holder for certain temperature-dependent measurements. The sample temperature at the bottom of the cold finger is monitored using a combination of LakeShore Cernox [1.40K to 325K] and Ruthenium Oxide - RuOx [42mK to 45K] sensors. Lock-in measurement of the resistance allows for the precise real-time monitoring of sample temperature, which is fully automated, with dynamic sensitivity and excitation voltage, using a QCoDeS [A.3]-based driver to avoid self-heating of the sensor resistor. Measurements were done with the sample mounted on the QDevil PCB for RF + DC measurements and, alternatively, an in-house sample holder with an LCC-20 chip carrier for DC and

low-frequency lock-in measurements. The RuOx and Cernox sensors and an Infrared LED are mounted at the bottom of the cold finger, as shown in [Fig. 7.2a]. The infrared LED is effective in increasing the carrier density in the 2DEG, consequently increasing the quality of contact with the 2DEG at base temperature in the case of GaAs|AlGaAs heterostructures. This is because the carriers in the quantum well are donated by the modulation-doped Si layer, which can get trapped in specific defect sites - DX centers. IR excitation allows these charges to cross the barrier at the heterostructure interface [Fig.2.3b] entering the quantum well.

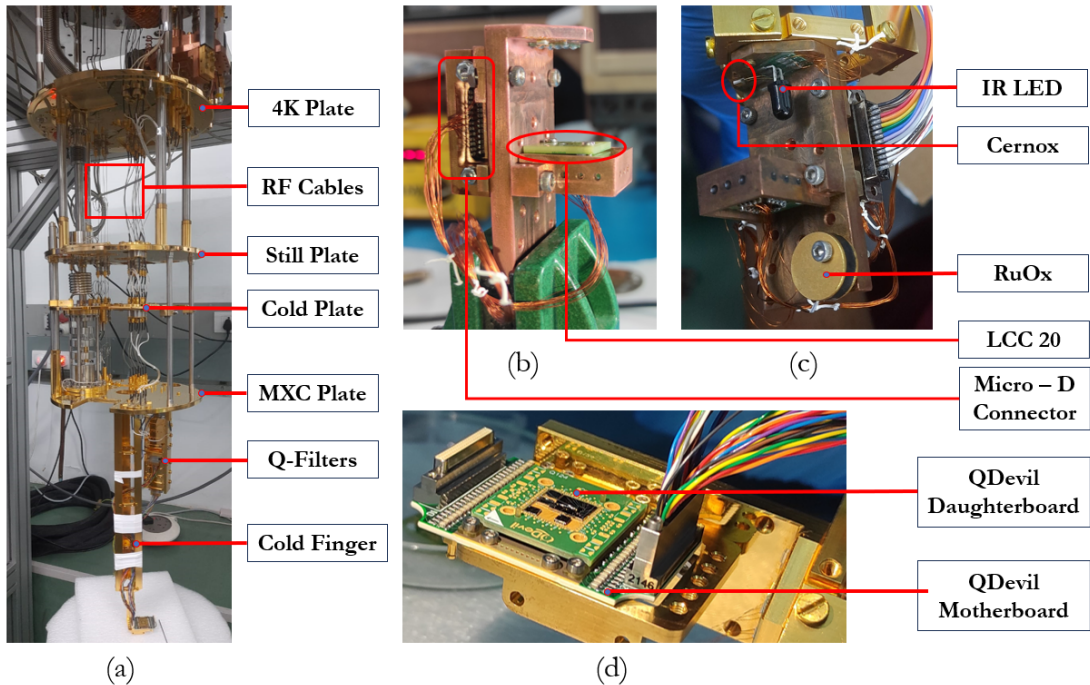


Figure 7.2: (a) Bluefors LD400. (b), (c) Images of the in-house DC sample holder with an LCC-20 chip carrier, IR LED, and RuOx and Cernox temperature sensors. (d) QDevil PCB (motherboard + daughterboard) for RF and DC measurements.

For low frequency or DC measurements, the QDevil motherboard PCB is equipped with 48 lines connected to bonding pads through the daughterboard. These lines have low-pass Q-filters to filter out high-frequency noise. Each Q-filter is an RF filter followed by an RC filter with cutoff frequencies 1.2 MHz and 62.5 kHz, respectively. 16 RF lines from mini-coax connectors are coupled capacitively through bias tees to combine with DC bias from 16 of the 48 DC lines. These are intended for the fast gates of the QD device.

Appendix A

Appendix

A.1 Quantum Hall Effect

This section is intended as a brief review primarily based on [25] of the theory behind the formulae applied to analyze experimental data in section 2.2.3.

Using the Drude model of electron transport, we can understand the origin of the transverse Hall voltage (V_H) in the presence of a perpendicular magnetic field. In presence of an out of plane magnetic field $\vec{B} = B\hat{z}$ and an electric $\vec{E} = E_x\hat{x} + E_y\hat{y}$ force on a charge carrier is given by:

$$\vec{F} = \vec{F}_{scat} + \vec{F}_{ext} = \frac{d\vec{p}}{dt}\Big|_{scat} + \frac{d\vec{p}}{dt}\Big|_{ext} \quad (\text{A.1})$$

The relaxation due to scattering is taken into account by incorporating a purely phenomenological constant τ . τ can be thought of as the rate at which a particle loses its momentum completely due to collision events, i.e., $\frac{d\vec{p}}{dt}\Big|_{scat} = -\frac{\vec{p}}{\tau}$. The external force $\vec{F}_{ext} = -e(\vec{E} + \vec{v} \times \vec{B})$ is the Lorentz force. The current density $\vec{j} = -en\vec{v}$. In steady state, $\vec{F} = 0$. This gives:

$$-e(E_x\hat{x} + E_y\hat{y}) = \frac{m}{\tau}(v_x\hat{x} + v_y\hat{y}) + eB(v_x\hat{y} - v_y\hat{x})$$

$$\begin{bmatrix} E_x \\ E_y \end{bmatrix} = \frac{m^*}{e^2 n \tau} \begin{bmatrix} 1 & -\omega_c \tau \\ \omega_c \tau & 1 \end{bmatrix} \begin{bmatrix} j_x \\ j_y \end{bmatrix} \quad (\text{A.2})$$

Here, $\omega_c = \frac{B}{m^* e}$ is the cyclotron frequency. m^* is the effective mass of the electron in the material. Since $\vec{E} = \vec{\rho} \leftrightarrow \vec{j}$, the longitudinal resistivity is a constant ($\rho_{xx} = \rho_{yy} = \sigma_D^{-1}$) whereas the transverse component is linearly dependent on magnetic field

$(\rho_{xy} = -\rho_{yx} = -\sigma_D^{-1} \frac{eB}{m^*})$. Here $\sigma_D = ne^2\tau/m^*$ is the Drude conductivity. For the configuration in figure (3.1), for weak magnetic field ($\omega_c\tau \ll 1$), in steady state, $j_y = 0$, and the fields E_x and E_y are assumed uniform. In that case, the measured voltages are $V_{xx} = E_x L$ and $V_{yx} = E_y W$. The current supplied I is known, thus, $j_x = \frac{I}{W}$.

$$\rho_{xx} = \frac{1}{\sigma_D} = \frac{V_{xx}W}{IL} \quad (\text{A.3})$$

$$\rho_{yx} = \frac{1}{\sigma_D} \frac{eB\tau}{m^*} = \frac{V_{yx}W}{IL} \quad (\text{A.4})$$

Knowing resistivity allows for calculating the carrier density n from the slope of the plot of ρ_{yx} vs B . The mobility can also be calculated as $\mu = |v_d/E_x|$: the ratio of the drift velocity to the electric field. The Hall voltage $V_{xy} = V_H$ is linearly dependent on B , whereas V_{xx} is a constant. This result only holds for low magnetic fields but hints at an essential property of the Hall effect. The Hall voltage is independent of the geometrical parameters L and W . Thus, if one were to make holes (somehow remove carriers) along the bulk of the channel, effectively changing w and L the longitudinal resistance would change, but the Hall voltage would remain unaffected.

The quantum mechanical treatment of the Hamiltonian of the system is needed to understand the features observed experimentally at high magnetic fields. The Hamiltonian in presence of a magnetic field $B\hat{z} = \vec{\nabla} \times \vec{A}$ is:

$$\hat{H} = \frac{1}{2m^*}(\vec{p} + e\vec{A})^2 = \frac{1}{2m^*}((p_x - eBy)^2 + p_y^2) \quad (\text{A.5})$$

Working in the Landau Gauge where $\vec{A} = (-By, 0, 0)$. Here, $[p_x, \hat{H}] = 0$, which implies translational invariance along the y direction, thus motivating the ansatz $\psi(x, y) = e^{ikx}\phi_k(y)$.

$$\hat{H}\psi_k(x, y) = \frac{1}{2m^*}[p_y^2 + (\hbar k - eBy)^2]\psi_k(x, y) = \hat{H}_k\psi_k(x, y) \quad (\text{A.6})$$

$$\hat{H}_k = \frac{1}{2m^*}p_y^2 + \frac{m\omega_c^2}{2}(y - kl_B^2)^2 \quad (\text{A.7})$$

Here, \hat{H}_k is the Hamiltonian of a simple harmonic oscillator displaced along the y -axis by kl_B^2 , where l_B is the magnetic length scale given by:

$$l_B = \sqrt{\frac{\hbar}{eB}} \quad (\text{A.8})$$

The energy eigenvalues and eigenfunctions are:

$$E_q = \hbar\omega_c \left(q + \frac{1}{2} \right) \quad (\text{A.9})$$

$$\tilde{\psi}_{q,k}(x, y) \sim e^{ikx} H_q(y - kl_B^2) e^{-(y - kl_B^2)^2 / 2l_B^2} \quad (\text{A.10})$$

H_q are Hermite polynomial eigenfunctions of the harmonic potential with $q \in \mathbb{N}$ and $k \in \mathbb{R}$. The energy levels depend only on q . Thus, the k values attainable contribute to the degeneracy of these states. The dimensions of the Hall bar are finite along the x and y directions, L and W , respectively. The momentum k is quantized in units of $2\pi/L$. Since $0 \leq y \leq W$, we expect $0 \leq k \leq W/l_B^2$ for the state to be localized around $y = kl_B^2$. Thus, the number of states is:

$$N(B) = \frac{L}{2\pi} \int_0^{W/l_B^2} dk = \frac{eBA}{2\pi\hbar} = \frac{AB}{\Phi_0} \quad (\text{A.11})$$

Here, $A = LW$ is the area, and the quantum of magnetic flux is defined as $\Phi_0 = \frac{2\pi\hbar}{e}$. The degeneracy of each Landau level is macroscopic. If the spin splitting is negligible, for carrier density n , nA electrons must be distributed between available Landau levels. Thus, the number of occupied Landau levels, also called the filling factor, is given by (labeled ν):

$$\nu = \frac{nA}{N} = \frac{nh}{eB} \quad (\text{A.12})$$

In the presence of an electric field $E\hat{y}$ in the y direction (analogous to Hall voltage), a term $\Phi_H = eEy$ must be added to the Hamiltonian. The procedure for solving the problem remains the same as above, just with an added term that acts like a shift of origin along the y -axis. The eigenstates and eigenenergies are now given by:

$$\psi(x, y) = \psi_{q,k}(x, y - mE^2/eB^2) \quad (\text{A.13})$$

$$E_{q,k} = \hbar\omega_c \left(q + \frac{1}{2} \right) - eE \left(kl_B^2 + \frac{eE}{m\omega_c^2} \right) + \frac{mE^2}{2B^2} \quad (\text{A.14})$$

The degeneracy of the Landau levels is now lifted since the energy depends on k . The x direction group velocity $v_x = \frac{1}{\hbar}\partial_k E_{q,k} = -E/B$ is nonzero.

To explain the experimentally observed Hall resistivity plateaus, we compute the current density for particles moving in a magnetic field when ν landau levels are filled (Fermi energy E_F is not overlapping with a Landau level):

$$\begin{aligned} \vec{J} &= -\frac{e}{mA} \sum_{\text{states}} \langle \psi | -i\hbar\vec{\nabla} + e\vec{A} | \psi \rangle \\ &= -\frac{e}{mA} \sum_{q=1}^{\nu} \sum_k \langle \psi_{q,k} | -i\hbar\vec{\nabla} + e\vec{A} | \psi_{q,k} \rangle \end{aligned} \quad (\text{A.15})$$

$$J_y = -\frac{e}{mA} \sum_{q=1}^{\nu} \sum_k \langle \psi_{q,k} | -i\hbar\partial_y | \psi_{q,k} \rangle = 0 \quad (\text{A.16})$$

Here, $\psi_{q,k}$ are the eigenstates obtained in equation A.10. The momentum expectation for harmonic oscillator states is zero.

$$\begin{aligned} J_x &= -\frac{e}{mA} \sum_{q=1}^{\nu} \sum_k \langle \psi_{q,k} | -i\hbar\partial_x - eBy | \psi_{q,k} \rangle \\ &= -\frac{e}{mA} \sum_{q=1}^{\nu} \sum_k \langle \psi_{q,k} | \hbar k - eBy | \psi_{q,k} \rangle = e\nu \sum_k \frac{E}{AB} \end{aligned} \quad (\text{A.17})$$

Since $\langle \psi_{q,k} | y | \psi_{q,k} \rangle = \hbar k / eB + mE / eB^2$ due to the effective origin shift. For $\vec{E} = E\hat{y}$ we get $\vec{J} = e\nu E / \Phi_0 \hat{x} = \vec{\sigma} \cdot \vec{E}$. This gives:

$$\sigma_{xx} = 0, \quad \sigma_{xy} = \frac{e\nu}{\Phi_0} \Rightarrow \rho_{xx} = 0, \quad \rho_{xy} = \frac{\Phi_0}{e\nu} = \frac{h}{e^2} \frac{1}{\nu} \quad (\text{A.18})$$

So far, we have ignored electron spin and disorders in the system. Spin splitting splits each Landau level into two, separated by $g\mu_B B$. Disorders are perturbations to the system that break the degeneracy of each Landau level. This leads to the broadening of each Landau level, forming bands. Disorders also lead to the localization of states around the disorder potential's extrema. These states are “stuck” to closed orbits around these extrema. Thus, extended states that move throughout the sample are guaranteed only at the edges along the equipotential contours (which are sparse in the bulk). Here, the underlying assumption is that the disorder potential V is much smaller than the landau level separation ($V \ll \hbar\omega_c$), and it varies only over length scales much larger than the magnetic length ($|\vec{\nabla}V|l_B \ll \hbar\omega_c$).

Conduction through these edge modes is key to the robustness of the Hall effect against disorders. Classically, in the presence of a strong magnetic field, electrons tend to follow “skipping orbits” along the two edges. The motion of the electrons along each edge is restricted in one direction, with the two edges having opposite chirality. In the absence of an electric field, the net current is zero. To understand the features of the ρ_{xx} and ρ_{yx} curves, consider a rectangular sample geometry finite along the y-axis (width W). The Hamiltonian then looks like:

$$\hat{H} = \frac{1}{2m^*}((p_x - eBy)^2 + p_y^2) + V(y) \quad (\text{A.19})$$

The eigenstates $\psi_{n,k}$ (eq A.10) are localized in the y direction on length scales of l_B around $x_0 = kl_B^2$, and thus for a smooth potential $V(y)$ effectively acts like an added

$\Phi = V(y_0) + \frac{\partial V}{\partial y}(y - y_0)$ term to the Hamiltonian. As seen previously (eq A.13), this just leads to a drift velocity along the x direction:

$$v_x = -\frac{1}{eB} \frac{\partial V}{\partial y} \quad (\text{A.20})$$

The drift is along $+x$ along one edge and $-x$ along the other. These are the so-called “skipping orbits”.

As discussed above, when the Fermi energy doesn't overlap with a Landau level, the conduction occurs via edge modes. On the contrary, when a broadened Landau level is partly filled (Fermi energy E_F lies within the Landau level), the electrons in the bulk can participate in conduction, leading to increased scattering and, thus, larger resistance. These jumps in resistance occur when the Fermi energy overlaps with a Landau level, which in turn depends on the magnetic field. When a Landau level is half-filled ($\nu = m/2 = nh/eB$ where $m \in \mathbb{N}$), a maximum in longitudinal resistance is seen. ρ_{xx} is periodic in $1/B$, allowing the calculation of number density as:

$$n = \frac{e}{h} \left(\frac{1}{\frac{1}{B_i} - \frac{1}{B_{i+1}}} \right) \quad (\text{A.21})$$

A.2 Reflectometry

Fast charge sensing by measuring the damping of a 1.7GHz resonant circuit was suggested by R. J. Schoelkopf et al. [6]. This allowed for high operation frequencies., much above the frequency regime where $1/f$ charge noise is prominent. The basic principle of reflectometry is the partial reflection of an AC signal in a transmission line due to impedance mismatch with the 50Ω transmission line impedance. This impedance, in turn, depends on the SET resistance. Most importantly, the apparatus is designed such that one can operate in the regime where the signal reflection is most sensitive to any impedance changes of the charge sensor SET.

The reflection coefficient for a signal of frequency ω labelled $\Gamma(\omega)$, for a transmission line with impedance Z_0 terminated by an impedance $Z = Z(\omega)$ is:

$$\Gamma(\omega) = \frac{Z(\omega) - Z_0}{Z(\omega) + Z_0} \quad (\text{A.22})$$

The reflected power $|\Gamma|^2$ is then a direct measure of Z . An indicator with impedance $X_L = R_L + i\omega L$ is used to form an LC circuit with the parasitic capacitance (C_p)

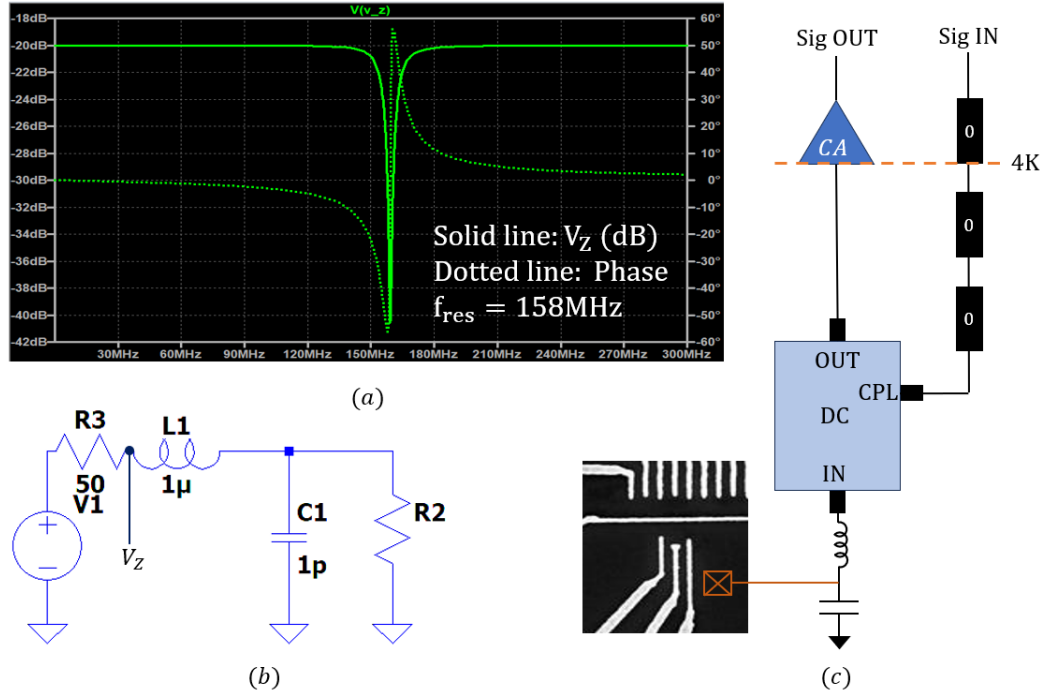


Figure A.1: (a) AC power at V_Z for different signal frequencies. A sharp dip in reflected power $\sim |\Gamma|^2$ is seen at a resonance frequency $\omega_{res} = 158\text{MHz}$ (b) The reflectometry circuit equivalent. (c) Circuit to be set up in the dilution refrigerator. CA: cryo-amplifier to amplify reflected signal. DC: directional coupler for selectively sending input signal to the sample and reflected output signal independently in respective RF lines.

of the line and the device (SET) capacitance. The components are chosen to allow for a sharp response of the circuit to change in sample impedance (R_D) at a fixed resonance frequency f_{res} of the order of 100MHz [Fig. A.1]. The total impedance of the circuit is:

$$\begin{aligned}
 Z(\omega) &= R_L + i\omega L + \frac{R_D}{1 + i\omega C_p R_D} \\
 &= R_L + \frac{R_D}{1 + \omega^2 C_p^2 R_D^2} + i \left(\omega L - \frac{\omega C_p R_D^2}{1 + \omega^2 C_p^2 R_D^2} \right) \\
 &\simeq R_L + \frac{R_D}{\omega^2 C_p^2 R_D^2} + i \left(\omega L - \frac{1}{\omega C_p} \right)
 \end{aligned} \tag{A.23}$$

Here, $\omega C_p R_D \gg 1$ since typically $\omega \sim 2\pi 100\text{MHz}$, $C_p \sim 1\text{pF}$, and $R_D \sim 100\text{k}\Omega$ (for a typical SET tuned to a few electron regime). At $\omega_{res} = 2\pi f_{res}$, we need the imaginary part to be 0 for the best possible impedance matching; thus, $\omega_{res} = \sqrt{LC_p}$. This gives $Z(\omega_{res}) \lesssim 20\Omega$ (for $L = \mu\text{H}$ and other parameters as stated above), which

indeed lies in the regime where Γ is highly sensitive to changes in Z .

The exact frequency ω_{res} is not important for charge sensing and is determined using a vector network analyzer (VNA) to do a frequency sweep and measure dip(s) in reflection coefficient S_{11} . The value of the inductor L is chosen such that given the knowledge of the approximate SET resistance and the parasitic capacitance, the resonance frequency lies in the range where it is within the bandwidth of the cryo-amplifier, attenuation along the RF lines is minimal and $1/f$ noise is negligible.

IQ modulation or high-frequency Lock-in techniques can be used to measure the phase and amplitude of the signal in reflectometry.

A.3 QCoDeS

QCoDeS is an open-source Python package developed by the Copenhagen / Delft / Sydney / Microsoft quantum computing consortium, made to facilitate data acquisition and handling for experiments in nanoelectronics. The drivers for the Lock-In amplifiers (SR-830, LIA-7265, LIA-7225), Stanford Research SIM-900 mainframe and associated modules, American Magnetics AMI 430, and Proteus 2588B -Arbitrary Waveform Generator were developed in-house using QCoDeS. Most instruments from Keysight, QDevil, and Keithley have well-tested drivers available on the QCoDeS GitHub page.

Bibliography

- [1] Graham Batey and Gustav Teleberg. Principles of dilution refrigeration.
- [2] C. W. J. Beenakker. Theory of coulomb-blockade oscillations in the conductance of a quantum dot. *Phys. Rev. B*, 44:1646–1656, Jul 1991.
- [3] Supriyo Datta. *Quantum Transport: Atom to Transistor*. Cambridge University Press, 2005.
- [4] David P. DiVincenzo. The physical implementation of quantum computation. *Fortschritte der Physik*, 48(9-11):771–783, sep 2000.
- [5] J. M. Elzerman, R. Hanson, L. H. Willems van Beveren, B. Witkamp, L. M. K. Vandersypen, and L. P. Kouwenhoven. Single-shot read-out of an individual electron spin in a quantum dot. *Nature*, 430(6998):431–435, jul 2004.
- [6] R. J. Schoelkopf et al. The radio-frequency single-electron transistor (rf-set): A fast and ultrasensitive electrometer. *Science*, 280(5367):1238–1242, 1998.
- [7] R. Hanson, L. P. Kouwenhoven, J. R. Petta, S. Tarucha, and L. M. K. Vandersypen. Spins in few-electron quantum dots. *Reviews of Modern Physics*, 79(4):1217–1265, oct 2007.
- [8] R. Hanson, L. H. Willems van Beveren, I. T. Vink, J. M. Elzerman, W. J. M. Naber, F. H. L. Koppens, L. P. Kouwenhoven, and L. M. K. Vandersypen. Single-shot readout of electron spin states in a quantum dot using spin-dependent tunnel rates. *Physical Review Letters*, 94(19), May 2005.
- [9] Manus Hayne, A USHER, J J HARRIS, and C T FOXON. Exchange enhancement of the landau-level separation for two-dimensional electrons in gaas/galxalxas heterojunctions. *Physical review B*, 46(15):9515–9519, October 1992. © 1992 The American Physical Society.

- [10] Jonathan Y. Huang et al. High-fidelity spin qubit operation and algorithmic initialization above 1 k. *Nature*, 627(8005):772–777, Mar 2024.
- [11] A Isihara and L Smrcka. Density and magnetic field dependences of the conductivity of two-dimensional electron systems. *Journal of Physics C: Solid State Physics*, 19(34):6777, dec 1986.
- [12] A. C. Johnson, J. R. Petta, C. M. Marcus, M. P. Hanson, and A. C. Gossard. Singlet-triplet spin blockade and charge sensing in a few-electron double quantum dot. *Physical Review B*, 72(16), October 2005.
- [13] K. v. Klitzing, G. Dorda, and M. Pepper. New method for high-accuracy determination of the fine-structure constant based on quantized hall resistance. *Phys. Rev. Lett.*, 45:494–497, Aug 1980.
- [14] Leo P. Kouwenhoven, Charles M. Marcus, Paul L. McEuen, Seigo Tarucha, Robert M. Westervelt, and Ned S. Wingreen. *Electron Transport in Quantum Dots*, pages 105–214. Springer Netherlands, Dordrecht, 1997.
- [15] N. S. Lai, W. H. Lim, C. H. Yang, F. A. Zwanenburg, W. A. Coish, F. Qassemi, A. Morello, and A. S. Dzurak. Pauli spin blockade in a highly tunable silicon double quantum dot. *Scientific Reports*, 1(1), oct 2011.
- [16] Daniel Loss and David P. DiVincenzo. Quantum computation with quantum dots. *Phys. Rev. A*, 57:120–126, Jan 1998.
- [17] Sudhasatta Mahapatra, Holger Büch, and Michelle Y Simmons. Charge sensing of precisely positioned p donors in si. *Nano letters*, 11(10):4376—4381, October 2011.
- [18] Michael J. Manfra. Molecular beam epitaxy of ultra-high-quality algaas/gaas heterostructures: Enabling physics in low-dimensional electronic systems. *Annual Review of Condensed Matter Physics*, 5(Volume 5, 2014):347–373, 2014.
- [19] D. Maradan, L. Casparis, T.-M. Liu, D. E. F. Biesinger, C. P. Scheller, D. M. Zumbühl, J. D. Zimmerman, and A. C. Gossard. GaAs quantum dot thermometry using direct transport and charge sensing. *Journal of Low Temperature Physics*, 175(5-6):784–798, apr 2014.

- [20] Michael A. Nielsen and Isaac L. Chuang. *Quantum Computation and Quantum Information: 10th Anniversary Edition*. Cambridge University Press, 2010.
- [21] Keiji Ono, Takahiro Mori, and Satoshi Moriyama. High-temperature operation of a silicon qubit. *Scientific Reports*, 9(1), Jan 2019.
- [22] John Preskill. Lecture notes for physics 229: Quantum information and computation, 1998.
- [23] C. B. Simmons, J. R. Prance, B. J. Van Bael, Teck Seng Koh, Zhan Shi, D. E. Savage, M. G. Lagally, R. Joynt, Mark Friesen, S. N. Coppersmith, and M. A. Eriksson. Tunable spin loading and T_1 of a silicon spin qubit measured by single-shot readout. *Phys. Rev. Lett.*, 106:156804, Apr 2011.
- [24] Gregory Snider. 1d poisson.
- [25] David Tong. Lectures on the quantum hall effect, 2016.
- [26] C. Volk et al. Loading a quantum-dot based “qubyte” register. *npj Quantum Information*, 5, 12 2019.
- [27] Gento Yamahata and al et. Control of electrostatic coupling observed for silicon double quantum dot structures. *Jpn. J. Appl. Phys.*, 47, 2008.
- [28] Jun Yoneda, Tomohiro Otsuka, Tatsuki Takakura, Michel Pioro-Ladrière, Roland Brunner, Hong Lu, Takashi Nakajima, Toshiaki Obata, Akito Noiri, Christopher J. Palmstrøm, Arthur C. Gossard, and Seigo Tarucha. Robust micromagnet design for fast electrical manipulations of single spins in quantum dots. *Applied Physics Express*, 8(8):084401, jul 2015.
- [29] D. M. Zajac, A. J. Sigillito, M. Russ, F. Borjans, J. M. Taylor, G. Burkard, and J. R. Petta. Resonantly driven CNOT gate for electron spins. *Science*, 359(6374):439–442, jan 2018.